Characterization of Microstructure Static Mixer Reactors: Transport Phenomena and Calorimetry for Mixing Limiting Reactions

James Adams

Thesis submitted to the University of Ottawa
in conformity with the requirements for the degree of Master of Applied Science

Department of Chemical and Biological Engineering, Faculty of Engineering, University of Ottawa

uOttawa

© James Adams, Ottawa, Canada, 2025

Abstract

The production of active pharmaceutical ingredients (APIs) is transitioning from conventional semi-batch processes towards continuous flow chemistry solutions. Continuous flow chemistry processes can be miniaturized and intensified to increase production quality and throughput. The smaller reactor volumes, in contrast to batchwise processes, have improved temperature control and diminish the risk and severity of accidents such as thermal runaways. Furthermore, continuous flow reactors can produce APIs that are ill-suited, difficult, or impossible to produce in conventional batchwise processes. Notably highly exothermic reactions at severe risk of thermal runaway, multiphase systems, and unstable products prone to decomposition or degradation.

In this study, the transport phenomena (frictional pressure loss, heat transfer, and residence time distribution) of a continuous flow shell and tube reactor are characterized for good manufacturing practices (GMP) production. The reactor features Kenics® static mixers to enhance the transport phenomena. The operating conditions and transport parameters were investigated in a dimensionless manner via friction factor, Nusselt and Peclet numbers. Empirical correlations are generated for the friction factor and inner tube Nusselt numbers covering tube diameters of 3.05 mm, which have not been reported in literature. The correlations generated accurate fits of the experimental data in the range of hydraulic Reynolds numbers ($200 < Re_h < 4500$) and Prandtl numbers ($4.6 < Pr < 7.0$). The residence time distribution (RTD) characterization found that the reactor is effectively plug flow as the Peclet number surpassed one hundred for the investigated power dissipations ($0.15\ W \cdot kg^{-1} < \varepsilon < 1.6\ W \cdot kg^{-1}$).

Furthermore, the heat of reaction for the synthesis of lithium diisopropylamine (LDA) from n-butyllithium (nBuLi) and diisopropylamine (DIPA) is estimated with a continuous calorimeter featuring a microstructure of static mixers. The LDA synthesis organolithium reaction is mixing limiting. The associated energy and species balance differential equations are solved with a MATLAB® simulation to obtain the heat of reaction. The heat of reaction is estimated to be between $-132\ kJ \cdot kg^{-1}$ and $-148\ kJ \cdot kg^{-1}$. The variation in the heat of reaction is presumed to occur from the significant variation in the local overall heat transfer coefficient along the reactor length. Suggesting that one or more thermal resistance undergoes substantial change. Of which the conductive resistances associated with the static mixer blade and thermocouple rod may be responsible.

Résumé

La production de principes actifs (PA) évolue des procédés conventionnels semi-discontinus vers des solutions en écoulement continu. Les procédés chimiques en continu peuvent être miniaturisés et intensifiés afin d'améliorer la qualité du produit et le rendement. En comparaison avec les procédés discontinus, les réacteurs des procédés continues ont des faibles volumes qui permettent un meilleur contrôle de température et réduisent les risques et la sévérité des accidents tels que les emballements thermiques. De plus, les réacteurs en écoulement continu permettent à la production de PA qui sont mal adaptés, difficiles ou même impossibles à produire par des procédés discontinus conventionnel. Cela concerne principalement les réactions fortement exothermiques présentant un risque élevé d'emballement thermique, les systèmes multiphasiques et les réactions qui génèrent des produits instables sujets à se décomposer.

Dans cette thèse, les phénomènes de transport (perte de charge par friction, transfert de chaleur et distribution de temps de séjour) d'un réacteur tubulaire en flux continu à double enveloppe sont caractérisés pour une production conforme aux bonnes pratiques de fabrication (BPF). Le réacteur est équipé de mélangeurs statiques de type Kenics® afin d'améliorer les phénomènes de transport. Les conditions opératoires et les paramètres de transport ont été étudiés avec des nombres sans dimension à l'aide du facteur de friction et le nombre de Nusselt et de Péclet. Des corrélations empiriques ont été établies pour le facteur de friction et le nombre de Nusselt dans le tube intérieur, avec un diamètre de 3,05 mm, ce qui n'est pas encore été rapporté dans la littérature. Ces corrélations démontrent une bonne concordance aux données expérimentales pour des nombres de Reynolds hydrauliques entre $200 < Re_h < 4500$ et des nombres de Prandtl entre $4,6 < Pr < 7,0$. La caractérisation de la distribution de temps de séjour (DTS) a identifié que le réacteur se comporte comme un écoulement piston, indiqué par le nombre de Péclet dépassant 100 pour les dissipations de puissance étudiées ($0,15\ W \cdot kg^{-1} < \varepsilon < 1,6\ W \cdot kg^{-1}$).

De plus, l'enthalpie de réaction du diisopropylamidure de lithium (LDA) a été estimée à l'aide d'un calorimètre en écoulement continu intégrant une micro-structure de mélangeurs statiques. La réaction organolithien de LDA est limitée par l'échange massique et réalisée à partir du n-butyllithium (nBuLi) et diisopropylamine (DIPA). Les équations différentielles des bilans d'énergie et de matière associées ont été résolues avec une simulation MATLAB® afin d'obtenir l'enthalpie de réaction. Celle-ci est estimée entre -132 $kJ \cdot kg^{-1}$ et -148 $kJ \cdot kg^{-1}$. La variation de

l’enthalpie de réaction est attribuée aux variations locales significatives du coefficient de transfert thermique global au long du réacteur. Ceci suggère qu’une ou plusieurs résistances thermiques subissent de changement notable. Les résistances conductrices associées aux mélangeurs statiques et aux thermocouples pourraient y être responsable.

Statement of Contributions and Collaborators

I hereby declare that I am the sole author of this thesis.

The thesis is written by me with editorial correction and feedback from Dr. Arturo Macchi, Dr. Jan Haelssig, and Dr. Dominique Roberge.

The second chapter of the thesis is written by me with editorial corrections from Dr. Arturo Macchi and Dr. Jan Haelssig. The experimental component of the work was performed be me in collaboration with Lonza Group AG under the supervision of Dr. Dominique Roberge.

The third chapter of the is written by me with editorial corrections from Dr. Arturo Macchi and Dr. Jan Haelssig. The experimental component of the work was performed by Lonza Group AG by Pierre-André Bregy under the supervision of Dr. Dominique Roberge. The continuous calorimeter used for the experimentation was provided by Fluitec AG and the overall heat transfer coefficients correlations and values were provided by Finn Steinemann.

Acknowledgements

I want to express my sincere gratitude to my supervisors Dr. Arturo Macchi, Dr. Jan Haelssig, and Dr. Dominique Roberge for the guidance, patience, encouragement and thoughtful input throughout this research project. Their invaluable expertise of microstructured reactors and thoughtful feedback were instrumental in refining the thesis. Furthermore, I want to thank the learning environment and commitment Dr. Macchi, Dr. Haelssig, and Dr. Roberge have fostered during my master thesis.

I would also like to thank the team I worked with at Lonza Group AG in Switzerland for their amazing support of my research, their feedback in refining the experimental protocols, and the welcoming environment they promote. I want to extend my gratitude to Dr. Bernhard Gutmann, Sarah Filliger, Christof Aellig, Irene Meier, and Dr. Petteri Elsner for all the support in the laboratory.

Furthermore, I want to acknowledge and thank Dr. Christopher Lan and Dr. Clémence Fauteux-Lefebvre for the time invested in being my master's defense committee. Reviewing and providing detailed feedback is a time-consuming task and I cannot be more grateful for their effort and investment.

Lastly, I want to thank my amazing partner, family, and friends for all their support, help, advice and understanding throughout the research and writing process of the master thesis. I want to thank my partner for her support during the internship in Switzerland and her commitment to visit during this period. I love you.

Table of Contents

List of Figures

List of Tables

Nomenclature and Symbols

Symbols		[Units]
General		
a	Shape factor	$[m^{-1}]$
A	Area	$[m^2]$
AARE	Average absolute relative error	[%]
A_c	Cross-section area	$[m^2]$
AIChE	American Institute of Chemical Engineers	[-]
AISI	American Iron and Steel Institute	[-]
API	Active pharmaceutical ingredients	[-]
A_s	Surface area	$[m^2]$
CFD	Computational fluid dynamics	[-]
C_i	Concentration of species *i*	$[mol \cdot s^{-1}]$
$\bar{C}_p$	Average specific heat capacity	$[J \cdot kg^{-1} \cdot K^{-1}]$
D	Inner diameter	[m]
D_a	Dispersion	$[m^2 \cdot s^{-1}]$
DAQ	Data acquisition	[-]
D_h	Hydraulic diameter	[m]
DIPA	Diisopropylamine	[-]
DIPPR	Design Institute for Physical Properties	[-]
E(t)	Residence time distribution	$[s^{-1}]$
E(θ)	Dimensionless residence time distribution	[-]
f	Darcy-Weisbach friction factor	[-]
F(t)	Cumulative fraction of tracer	[-]
F(θ)	Dimensionless cumulative fraction of tracer	[-]
F_i	Molar flow rate	$[mol \cdot s^{-1}]$
GMP	Good manufacturing practices	[-]
h_i	Inner heat transfer coefficient	$[W \cdot m^{-2} \cdot K^{-1}]$
h_o	Outer heat transfer coefficient	$[W \cdot m^{-2} \cdot K^{-1}]$
H_{rx}	Heat of reaction	$[J \cdot mol^{-1}]$ or $[kJ \cdot kg^{-1}]$
HTM	Heat transfer medium	[-]
k	Thermal conductivity	$[W \cdot m^{-1} \cdot K^{-1}]$
K_f	Fluid thermal conductivity	$[W \cdot m^{-1} \cdot K^{-1}]$
k_{mix}	Mixing rate constant	$[s^{-1}]$
k_o	Overall reaction rate constant	$[s^{-1}]$
k_r	reaction kinetic constant	$[s^{-1}]$
L	Length	[m]
LDA	Lithium diisopropylamine	[-]
$\dot{m}$	Mass flow rate	$[kg \cdot s^{-1}]$
nBuLi	n-butyllithium	[-]
$\overline{Nu}$	Average Nusselt number	[-]
Nu	Nusselt number	[-]
ODE	Ordinary differential equation	[-]
ΔP	Frictional pressure drop	[Pa]

Pr	Prandtl number	[-]
PTFE	Polytetrafluoroethylene	[-]
$\dot{Q}$	Volumetric flow rate	[$m^3 \cdot s^{-1}$]
Q_c	Heat flow exchanged	[W]
Q_m	Heat flow of mass	[W]
Q_r	Heat flow of reaction	[W]
R&D	Research and development	[-]
Ra	Aspect ratio	[-]
Re	Reynolds number	[-]
Re_h	Hydraulic diameter Reynolds number	[-]
r_i	Reaction rate of species *i*	[$mol \cdot m^{-3}$]
RTD	Residence time distribution	[-]
R_{wall}	Wall heat transfer resistance	[$W \cdot m^{-1} \cdot K^{-1}$]
S&T	Shell and tube	[-]
T	Temperature	[°C]
t	Time	[s]
T-I-S	Tank-in-series	[-]
THF	Tetrahydrofuran	[-]
t_m	Mean residence time	[s]
$\bar{u}$	Average superficial velocity	[$m \cdot s^{-1}$]
u	Superficial velocity	[$m \cdot s^{-1}$]
$\bar{U}$	Average overall heat transfer coefficient	[$W \cdot m^{-2} \cdot K^{-1}$]
U	Overall heat transfer coefficient	[$W \cdot m^{-2} \cdot K^{-1}$]
V_R	Reactor interstitial volume	[m^3]
w	Blade thickness	[m]
X	Reaction Conversion	[%]
z	Axial length	[m]
Greek Symbols		
σ_t^2	Variance	[s^2]
σ_θ^2	Dimensionless variance	[-]
ε	Energy dissipation	[$W \cdot kg^{-1}$]
θ	Dimensionless mean residence time	[-]
ρ	Density	[$kg \cdot m^{-3}$] or [$g \cdot mL^{-1}$]
τ	Nominal space time	[s]
ϕ	Void fraction	[-]
Subscripts		
∞	Refers to the coolant fluid	[-]
i	Refers to the inner tube	[-]
In	Refers to the inlet	[-]
j	Refers to the jacket	[-]
LMTD	Log-mean temperature difference	[-]
Max	Maximum	[-]
Min	Minimum	[-]
o	Refers to the outer tube	[-]
OO	Open-open boundary conditions	[-]

Out	Refers to the outlet	[-]

1. Introduction

Continuous flow chemistry is becoming increasingly important for the pharmaceutical industry. The production of active pharmaceuticals ingredients (APIs) has been transitioning from the dominant conventionally used (semi)-batch processes to flow chemistry solutions. This paradigm shift in API production has been associated with the numerous advantages of continuous processes. Notably the processes can be miniaturized and intensified based on process intensification principles to increase throughput and product quality[1–3]. Furthermore, the process operation is safer as the operators contact with chemicals is reduced and the smaller reactor volume reduces the risk and severity of accidents such as runaway conditions or explosions[4–6]. In addition, the smaller reactor scales improve the temperature control of the reactor[7,8]. However, the most important advantage is the ability to produce APIs that are ill-suited or impossible to produce in batchwise processes[9,10]. Some of these ill-suited reactions are highly exothermic reactions with severe risks of thermal runaway, multiphase reaction mixtures, or unstable products prone to degradation impacting yields.

The scale-up of micro-reactor relies heavily on the heat transfer potential of the reactor at larger scales[11]. This is due to the sharp decrease in the surface-to-volume ratio from the plate reactors up to larger shell and tube reactors. This heavily reduces the cooling efficiency of larger reactors, potentially impacting the temperature profile inside of the reactor. This may worsen the broadness and magnitude of the hotspot impacting negatively the yield and selectivity of the reaction. Previous work in micro-reactor has demonstrated the benefits of scaling the reactors based on micromixing intensity[12,13]. The constant micromixing intensity or power dissipation is critical for relatively fast reactions, allowing for the overall reaction kinetic response to remain identical. In all cases, identical residence times distributions are required to maintain the reaction conversion. Specific to this field of study, to facilitate the reactor design of continuous flow reactors for API production, the reactions are classified based on their characteristic reaction time. The four classifications are type A, B, C, and D[14–16]. Type A reaction classified as mixing controlled reactions due to their reaction times below 1 second. These reactions are prone to hotspot formation increasing side-products from parallel-competitive reactions. Temperature control and reactant stoichiometry must be highly optimized to prevent selectivity losses. Type B reactions are classified by a longer reaction time ranging from 1 second to 10 minutes. These reactions are kinetically dominant and benefit from the increased heat transfer provided by intensified

continuous processes. Type C reactions have reaction time greater than 10 minutes and have hazardous tendencies. They are best suited for batch processes however continuous processes offer significant safety or production benefits. Type D reactions are all remaining reactions not encompassed by the other types. These reactions are candidates for process intensification benefits such as increased reaction temperatures and pressures. In this thesis, the organolithium reagents investigated are type A reactions.

Scaling the reactor by maintaining constant power dissipation and mean residence time ensures the pressure resistance is similar at the different reactor scales. However, to sustain power dissipation at larger scales, the volumetric flow rates inside the reactor must be increased accordingly. This larger volumetric flow rates impact the temperature control of the reactor as reaction heat scales volumetrically while the heat removed by cooling scales with the tube surface area. The loss of surface-to-volume ratio is a key challenge in scaling up highly exothermic reactions.

For exothermic reactions, design solutions have been developed to reduce the loss of heat transfer that occurs from the increased tube scale. The multi-injection principle is one solution[17,18]. The multi-injection principle fractionates the reaction mixture along the length of the reactor instead of being concentrated at the reactor inlet. The fraction of the reaction mixture and injection locations are thus selected to reduce the reaction rate and thus reduce the hotspot magnitude. Hence, prevents degradation and side-product formation and distributes the heat load throughout the reactor. However, this approach is ill-suited for reaction networks where the product is reactive with the starting material, or for unstable products as the injections (e.g., first vs last) extends their residence time in the reactor promoting additional degradation. Alternatively, solutions from the bulk industrial industries such as shell & tube reactor are applicable. These solutions are focused on increasing the heat transfer capacity of the reactor by optimizing the reactor design. This can be performed by adjusting the reactor operation such as diluting the reaction mixtures to decrease the heat load in the reactor, or by adjusting the reactor network to have multiple reactors operating in parallel (e.g. numbering up) effectively splitting the heat load.

1.1. Research Objectives

The objectives of this thesis is to characterize the transport phenomena (frictional pressure loss, heat transfer, and residence time distribution) of a continuous flow shell and tube reactor and

determine the heat of reaction of lithium diisopropylamine (LDA) investigated and reported in a continuous flow calorimeter. In both the continuous calorimeter and the shell and tube reactor, static mixer microstructures are added to improve both mixing rate and heat transfer in the system.

Chapter 2 of the thesis focuses on the transport phenomena characterization of the shell and tube reactor. The characterization is performed on two distinct experimental setups, the first is designed to determine both frictional pressure loss and fluid-to-wall heat transfer, while the second experimental setup characterizes the fluid residence time distribution. The operating conditions and transport parameters are investigated in a dimensionless manner via friction factor, Nusselt and Peclet numbers. These were then applied to generate coefficients for empirical correlations suitable for tube diameters and Kenics® mixer diameters that have not been reported in literature. Lastly, the transport phenomena were related to the power dissipation to understand the challenges and expected behaviours of an up-scaled shell and tube reactor applied for GMP production of an API.

Chapter 3 is aimed at determining the heat of reaction of lithium diisopropylamine (LDA) in the continuous flow calorimeter. The synthesis of LDA is produced by an organolithium reaction between n-butyllithium (nBuLi) and diisopropylamine (DIPA). The LDA reaction behaves as a type A reaction as the reaction time is less than one second. The heat of reaction is calculated by solving the energy and the associated species balances differential equations with a MATLAB® simulation. The LDA reaction kinetic model is examined under mixing limiting conditions. The heat of reaction is evaluated at different flow rates and overall reaction kinetic constants. Lastly, the heat of reaction's best fit from the MATLAB® simulation is compared with heat of reaction obtained by following the discrete heat model outlined in Steinemann et al.[19]. The limitations and advantages of both methodologies are discussed.

2. Microstructure Static Mixer Reactor Transport Phenomena Characterization using Modern Tools.

2.1. Introduction

Continuous flow chemistry is becoming increasingly important for the pharmaceutical industry. The production of active pharmaceuticals ingredients (APIs) has been transitioning from the dominant conventionally used (semi)-batch processes to flow chemistry solutions. This paradigm shift in API production has been associated with the numerous advantages of continuous processes. Notably the processes can be miniaturized and intensified based on process intensification principles to increase throughput and product quality[1,2]. Furthermore, the process operation is safer as the operators contact with chemicals is reduced and the smaller reactor volume reduces the risk and severity of accidents such as runaway conditions[4]. However, the most important advantage is the ability to produce APIs that are ill-suited or impossible to produce in batchwise processes[9]. Some of these ill-suited reactions are highly exothermic reactions at severe risk of thermal runaway, multiphase reaction mixtures, or unstable products decomposition impacting yields.

The research and development (R&D) of continuous flow reactors is performed at various reactor scales before finalizing the production process. The process development from the laboratory scale to production is done with micro-scale reactor. Micro-reactors have larger heat transfer rates and require little starting material, both advantages when the material is limited and expensive to produce[20]. The reaction kinetic conditions can be initially investigated in plate-type reactors before advancing to a laboratory scale shell and tube reactor.

The scale-up of micro-reactor relies heavily on the heat transfer potential of the reactor at larger scales[11]. This is due to the sharp decrease in the surface-to-volume ratio from the plate reactors up to larger shell and tube reactors. This heavily reduces the cooling efficiency of larger reactors, potentially impacting the temperature profile inside of the reactor. Previous work in micro-reactor has demonstrated the benefits of scaling the reactors based on micromixing intensity[12,13]. The constant micromixing intensity or power dissipation is critical for relatively fast reactions, allowing for the overall reaction kinetic response to remain identical. In all cases, identical residence times distributions are required to maintain the reaction conversion.

Scaling the reactor by maintaining constant power dissipation and mean residence time ensures the pressure resistance is similar at the different reactor scales. However, to sustain power dissipation at larger scales, the volumetric flow rates inside the reactor must be increased accordingly. This larger volumetric flow rates impact the temperature control of the reactor as reaction heat scales volumetrically while the heat removed by cooling scales with the tube surface area. The loss of surface-to-volume ratio is a key challenge in scaling up highly exothermic reactions.

In this work, transport phenomena (frictional pressure loss, heat transfer, and residence time) of a continuous flow shell and tube reactor are characterized. The characterization is performed on two distinct experimental setups, the first is designed to determine both frictional pressure loss and fluid-to-wall heat transfer, while the second experimental setup characterizes the fluid residence time distribution. The reactor features Kenics® static mixers to enhance the transport phenomena. The operating conditions and transport parameters were investigated in a dimensionless manner via friction factor, Nusselt and Peclet numbers. These were then applied to generate coefficients for empirical correlations suitable for tube diameters and Kenics® mixer diameters that have not been reported in literature. Lastly, the transport phenomena were related to the power dissipation to understand the challenges and expected behaviours of an up-scaled shell and tube reactor applied for GMP production.

2.2. Equipment & Procedure

2.2.1. Equipment and Operating Conditions

2.2.1.1. Heat Transfer & Frictional Pressure Drop

The heat transfer and pressure drop characterization was performed in a customized shell and tube reactor manufactured by Lonza Group AG. A shell and tube reactor was chosen for the characterization as a production-scale reactor was developed with the laboratory results. This allows the reactor's geometrical shape and technology to be maintained between scales. The reactor length is 4800 mm, and the nominal diameter of the shell is 157 mm, and the tubes 6.35 mm. The reactor has sixteen tubes where ten have an inner diameter of 4.57 mm, and six with inner diameters of 3.05 mm. The shell-side features three baffles with a height of 109 mm, occupying 74.2% of the shell cross-sectional area, distanced at 100 mm from each other. The shell and tube

reactor was operated co-currently and constructed in stainless steel (AISI 316). The thermal conductivity of stainless steel is taken as 15 $W \cdot m^{-1} \cdot K^{-1}$.

Static mixers were added to the reactor tubes to promote both heat transfer and mixing. The static mixers are Kenics® type and manufactured by JLS International. They have a nominal diameter of 2.90 mm, a unit length of 4.30 mm corresponding to an aspect ratio (Ra) of 1.5, a blade thickness of 0.7 mm, and a corresponding hydraulic diameter of 1.45 mm (for a tube diameter of 3.05 mm). The mixers occupy the entirety of the tube length and have a measured void fraction of 84%. The elements are constructed of stainless steel (AISI 316). The shell and tube design allows for rapid removal or addition of static mixers.

The heat transfer and pressure drop characterization was performed in a closed loop system, see Fig. 2-1. The fluid was pumped by an Ismatec® gear pump from the vessel to be pre-heated to 40°C in a coil by a Huber Ministat 230. The hot fluid enters the reactor and is cooled by the ethanol on the shell side at 5°C. A Huber CC55W thermoset and Huber MC24x1.5 pump were used for the cooling fluid cycle. The ethanol flow rate is 572 $L \cdot h^{-1}$ in the shell, sufficient to prevent large temperature differences between the coolant between the inlet and outlet. Temperature sensors, Pt100, and pressure probes, WIKA 0-6 bar, are situated at the inlet and outlet of the reactor. The pressure probes are positioned at the inlet and outlet of the reactor to prevent any interferences from the temperature probes. Furthermore, the thermocouple is positioned in a side-on manner to have the most precise temperature measurement[21]. The data acquisition system is managed by HiTec Zang allowing the collection of data every half second. The system fittings are Swagelok. The material of construction for the hard tubing is stainless steel (AISI 316) and soft tubing is in PTFE.

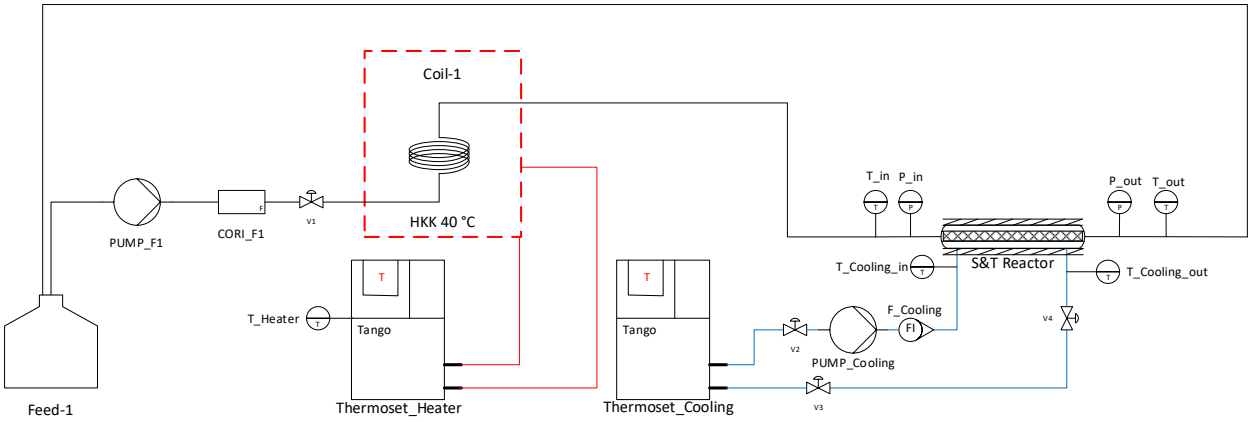

Fig. 2-1: Heat transfer and frictional pressure drop experimental setup.

2.2.1.2. Residence Time Distribution

The residence time distribution was determined by a density step change experiment. The step change was performed by switching the feed fluid from a low-density fluid to a high-density fluid. The selected fluids, THF and heptane, have sufficiently different densities allowing the Coriolis (Endress + Hauser Promass 80A) to accurately detect the density step change. Additionally, the organic solvents were selected as they do not exhibit strong surface tension or miscibility issues during a step change. This was verified experimentally by performing the step change with pure THF and heptane and a step change with an 80-20 wt.% mixture of the solvents. The two fluids are pumped independently by Masterflex® Ismatec® gear pumps into a four-way pneumatic valve. The valve rotates between two positions allowing either the THF or the heptane to flow in the reactor tube, while the other fluid goes to waste, see Fig. 2-2. The waste container was inerted with nitrogen to maintain a non-flammable atmosphere. To isolate the RTD characteristics of the reactor and avoid distortions from the transport lines, the fluids density was recorded at the inlet and the outlet of the reactor[22]. The instrumentation choice of a Coriolis for the RTD measurement was made as they are GMP certified, easy to install and remove for testing, and easy to procure. Additionally, the Coriolis measures the cross-sectional average value of the density allowing for a mixing cup measurement of the RTD[22]. The instruments interact with the HiTec Zang lab manager and software for data acquisition.

The RTD characterization is performed on a single tube with a length of 480 mm, a nominal and inner diameter of 6.35 mm and 3.05 mm, respectively. The tube is constructed in AISI 316 stainless steel. The solvents are kept at ambient temperature and pressure. Static mixers are added to the

tube for the RTD characterization. The static mixers are identical to the ones used in the shell and tube (S&T) temperature and pressure characterization. They have a nominal diameter of 2.90 mm, a unit length of 4.30 mm, aspect ratio (Ra) of 1.5, a blade thickness of 0.7 mm, and a corresponding hydraulic diameter of 1.45 mm (for tube diameters of 3.05 mm). The mixers occupy the entirety of the tube length and have a measured void fraction of 84%. The reactor volume with mixers is measured experimentally by water displacement to be 2.9 mL. The elements are constructed of stainless steel (AISI 316).

The residence time of the reactor is investigated at different mass flow rates. The flow rates of both solvents are kept identical during the characterization. This is performed to minimize disturbances in the flow regime of the reactor which may convolute the step change. The flow rates for the characterization being at 20 $g \cdot min^{-1}$ increasing by intervals of 5 $g \cdot min^{-1}$ up to a maximum flow rate of 55 $g \cdot min^{-1}$. Increasing the flow rate past 55 $g \cdot min^{-1}$ is not feasible as the Coriolis response time of 0.5 seconds is not sufficient to accurately measure the transient density change.

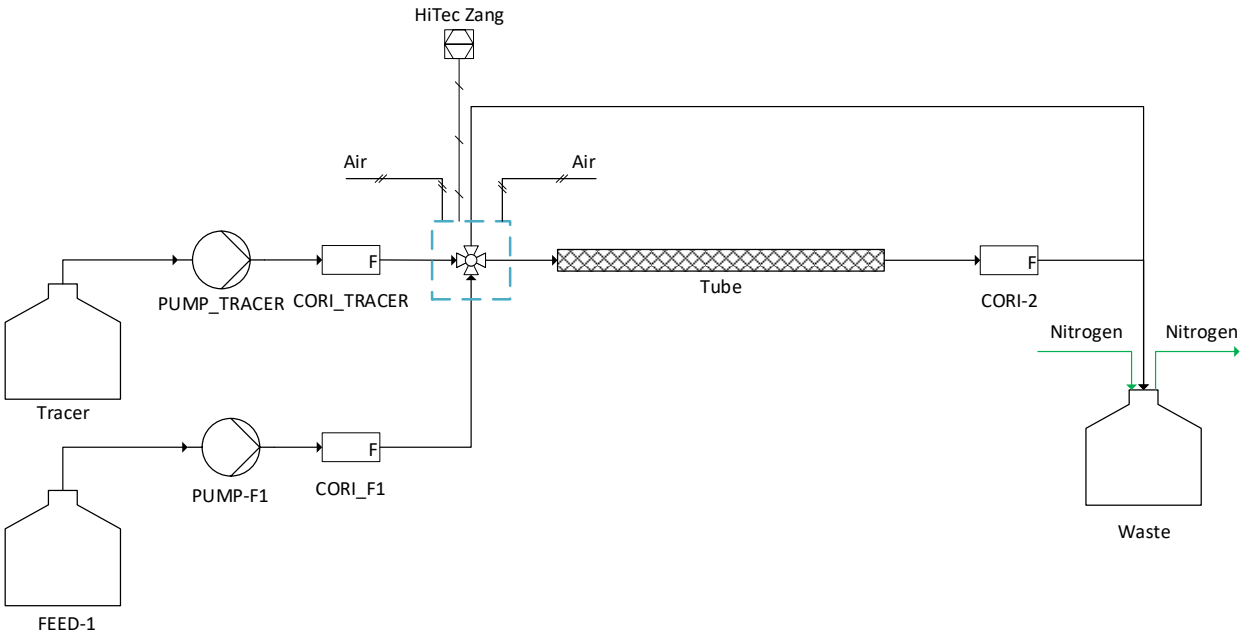

Fig. 2-2 : Residence time distribution experimental setup.

2.2.2. Numerical Methodology

2.2.2.1. Frictional Pressure Drop

The friction pressure drop in the horizontal tubes of the shell & tube reactor is obtained by a mechanical energy balance and expressed by the Darcy-Weisbach equation.

$$\Delta P = f\rho\frac{\bar{u}^2}{2}\frac{L}{D_h} \qquad (1)$$

The friction factor is a function of both the Reynolds (Re) number and the pipes relative roughness[23]. For smooth pipes, the friction factor can be estimated based on the Hagen-Poiseuille equation, $f = \frac{64}{Re}$ $(Re < 2000)$, if laminar, or the Blasius equation, $f = \frac{0.3164}{Re^{0.25}}$ $(4000 < Re < 10^5)$, when turbulent. In empty tubes, Reynolds under 2000 is laminar, between 2000 and 5000 are in a transition between laminar and turbulent, and above 5000 turbulent. In pipes with static mixers, the critical Reynolds numbers for laminar to turbulent flow transition differs from those set for empty tubes. The complex geometry of the mixers (aspect ratio, blade thickness, twist angles), as well as mixer specific features (SMX, Kenics®) generate secondary flow structures that disrupt the empty tube flow field. Generally for Kenics® mixers, laminar conditions are defined up to a Reynolds of 50, while turbulent regime is achieved with Reynolds above 1000[24–26]. However, for a given static mixer design, the cutoff ranges may differ, such as Sir and Lecjaks where they reported a fully turbulent regime when Re > 2000[26]. The friction factor is empirically defined under a generalized expression (Eq. (2)) for static mixers. The first form is focused on the transitional flow regime, while the second form is used for packed beds where the first term is the laminar contribution and the second term the turbulent contribution[24–29].

$$f = \frac{a}{Re^b} \; or \; f = \frac{c}{Re} + d \qquad (2)$$

Where *a*, *b*, *c,* and *d* are empirical coefficients optimized based on the specific Reynolds ranges, mixer design, and fluids. The friction factor correlation values respect the Darcy-Weisbach definition. Additionally, friction factors coefficients can be reported based on the inner tube diameter Reynolds number or the hydraulic diameter Reynolds number (Re_h). The hydraulic diameter is directly related to the geometry of the mixer at hand, for a Kenics® mixer the hydraulic diameter analytical solution is defined in equation (3). A list of friction factor coefficients found in literature is listed in Table 2-1 with the ranges of Reynolds and mixer geometry investigated. For our correlation development, the friction factor model with parameters *c* and *d* will be used for the structured reactors (akin to packed beds) and will be based on the hydraulic Reynolds number[24,30,31].

$$d_h = \frac{\pi D - 4w}{\pi + 2 + 2w/D} \quad (3)$$

Table 2-1: Kenics® mixer friction factor empirical correlations coefficients from literature.

Source	Reynolds range	Mixer geometry	*a*	*b*	*c*	*d*
Joshi et al.[27]	$10 < Re_h < 10{,}000$	D: 20 mm; Ra: 1.5, 2, 2.5; w: 1.5 mm	$30.3Ra^{-1.04}$	0.488	-	-
Morris and Benyon[28]	$Re_h < 6000$ $6000 < Re_h < 30000$	D: 12.7 mm; Ra: 2.5	12.6 1.1	0.5 0.11	-	-
Sir and Lecjak[26]	$10^{-2} < Re < 10^4$	**Mixer 1:** D: 21 mm; Ra: 2; w: 2 mm **Mixer 2:** D: 30 mm; Ra: 2 mm; w: 3 mm Twist angle 180°	-	-	85.5	0.3375
Song and Han[29]	$Re/Ra^{2.15} < 100$ $100 < Re/Ra^{2.15} < 1000$ $1000 < Re/Ra^{2.15}$	D: 4.93 mm, 8.1mm, 10.92 mm; Ra: 1.74, 1.67, 1.8	$320/Ra^{0.191}$ $32/Ra^{1.266}$ $2.66/Ra^{2.04}$	0.86 0.36	-	-
Hosni et al.[24]	$8111 < Re < 18940$	D: 40 mm, Ra: 1.5, w: 2 mm, 1 to 6 elements	195	0.74	-	-

The experimental friction factor of the reactor is calculated by re-arranging the pressure drop equation for the friction factor. The experimental work varied the fluid flow rate and type of fluid used during the analysis, both embedded in the hydraulic Reynolds number. The range of hydraulic Reynolds numbers tested was from 200 to 4500, encompassing the transition regime and fully turbulent regime expected in Kenics® mixers. The fluids investigated were THF and water for their substantial differences in density.

The power dissipation per unit mass is determined experimentally from pressure drop data and the nominal space time (or mean residence time) and serves as the key scale-up factor in this work. This scaling factor is selected because of the mixing-limited conditions of the type A reactions; thus, it is essential to maintain the mass transfer at different scales. Power dissipation is a measure of the convective mixing and formation of vortices within the reactor tubes, directly influencing micromixing time scale[12]. By holding the power dissipation constant across various reactor scales, micromixing conditions are identical, which is vital for the scale-up of mixing-limited reactions. Power dissipation is intrinsically linked to the pressure drop of the system, with an increase in pressure drop leading to proportional growth in mixing intensity and power dissipation.

$$\varepsilon = \frac{\Delta P \dot{Q}}{\rho V_R} = \frac{\Delta P \bar{u}}{\rho \mathrm{L}} = \frac{\Delta P}{\rho \tau} \quad (4)$$

The experimental trial conditions are listed in Table 2-2. The number of tubes used for the reactor pressure evaluation is tested with one and three tubes. This experimental choice is to evaluate the pressure drop with increasing length, but secondly to investigate if developing flow conditions (i.e. entrance effects) are present. Indications of developing flow will be evident if the pressure drop trends are not consistent between the single tube and multi-tube trials. The fluid variation is included to account for different fluid properties.

Table 2-2: Frictional pressure drop and heat transfer experimental trials conditions for reactor tubes (single tube length 0.48 m) featuring Kenic® static mixers. Inlet temperature of inner tube set at 40°C and heat transfer medium (HTM) at 5°C.

Trial identification	Tube count	Fluid	Flow rate	Re_h	Pr
	[#]		[g·min^{-1}]		
7340-09	1	Water	170-900	493-4356	4.59-5.25
7340-11	3	Water	57-517	201-2282	5.09-6.56
7340-12	1	Water	57-900	224-4330	4.62-5.82
7340-13	1	THF	43-554	306-4491	6.41-6.88
7340-14	3	THF	43-554	281-3454	6.65-6.96

2.2.2.2. Heat Transfer

To characterize the heat transfer in the reactor, the overall heat transfer coefficient must be determined with the generalized energy balance. The experimental protocol is designed to have heat transfer occur between the inner tube fluid and the coolant fluid on the outer tube. The system is inert removing the heat of reaction term for the energy balance. The reactor features insulation on the outside of the shell to minimize heat gain from the environment.

$$\bar{U}_i = \frac{\dot{m}\bar{C}_p(T_{in} - T_{out})}{A_i \Delta T_{LMTD}} \tag{5}$$

$$\Delta T_{LMTD} = \frac{(T_{in} - T_{\infty,in}) - (T_{out} - T_{\infty,out})}{\ln\left(\frac{T_{in} - T_{\infty,in}}{T_{out} - T_{\infty,out}}\right)} \tag{6}$$

The overall heat transfer coefficient obtained from the energy balance is averaged over the entire reactor length. This average overall heat transfer coefficient is obtained as the reactor temperature profile is only measured at the inlet and outlet of the reactor. The overall heat transfer can be split into the three heat transfer mechanisms found in the shell & tube reactor. The inner and outer convective heat transfer coefficients, and the reactor wall conductive resistance.

$$\bar{U}_\iota = \frac{1}{\frac{1}{\bar{h}_i} + R_{wall}A_i + \frac{A_o}{A_i \bar{h}_o}} \qquad (7)$$

The overall heat transfer equation can be linearized such that the inner heat transfer coefficient is able to be determined from the experimental data collected[12]. To determine the inner heat transfer coefficient, the outer heat transfer coefficient and the wall conductivity were constant and their resistances intended to be non-governing. For the outer heat transfer coefficient this was achieved by adjusting the HTM flow rate to a fixed value such that coolant temperature remained constant between the inlet and the outlet. The wall resistance is dependent on the thickness and thermal conductivity of the tube. These properties are constant for the given tube investigated but will differ if the tube diameters are altered.

$$\frac{1}{\bar{U}_\iota} = \frac{1}{\bar{h}_i} + \beta$$
$$where\ \beta = R_{wall}A_i + \frac{A_o}{A_i \bar{h}_o} \qquad (8)$$

To relate the overall heat transfer with the hydraulic Reynolds number, the inner heat transfer coefficient is replaced with the inner Nusselt number. The inner Nusselt number is influenced by the hydraulic Reynolds number and the Prandtl number of the fluid. The fluid properties variation is negligible in the experimental trials allowing the Prandtl number to be treated as a constant. The relationship between the average overall heat transfer coefficient and the hydraulic Reynolds number is obtained by combining equations (9) and (10).

$$\overline{Nu}_i = \frac{\bar{h}_i D_i}{k} = \text{fnct}(\text{Re}_\text{h}, \text{Pr}) \qquad (9)$$

$$\frac{1}{\bar{U}_\iota} = \frac{D_i}{Ck}\frac{1}{Re_h} + \beta \qquad (10)$$

$$\overline{Nu}_\text{i} = \frac{D_i}{k\left(\frac{1}{\bar{U}_\iota} - \beta\right)} \qquad (11)$$

For the development of coefficients for empirical correlations, the experimental Nusselt number must be determined. By re-arranging equation (8) the Nusselt number is isolated. The β-coefficient must be determined by plotting $1/\bar{U}_\text{i}$ versus $1/\text{Re}_\text{h}$ and determining the associated intercept of the linear regression (Fig. 2-3)[12].

Determining the inner heat transfer coefficient by plotting $1/\bar{U}_i$ vs. $1/Re_h$ is advantageous as additional models for the outer tube and wall resistances are not needed. The contributions of the different heat transfer mechanisms can be determined afterwards, by assuming a heat transfer model for wall resistance. This analysis is applied to determine which heat transfer mechanisms are rate governing in the system.

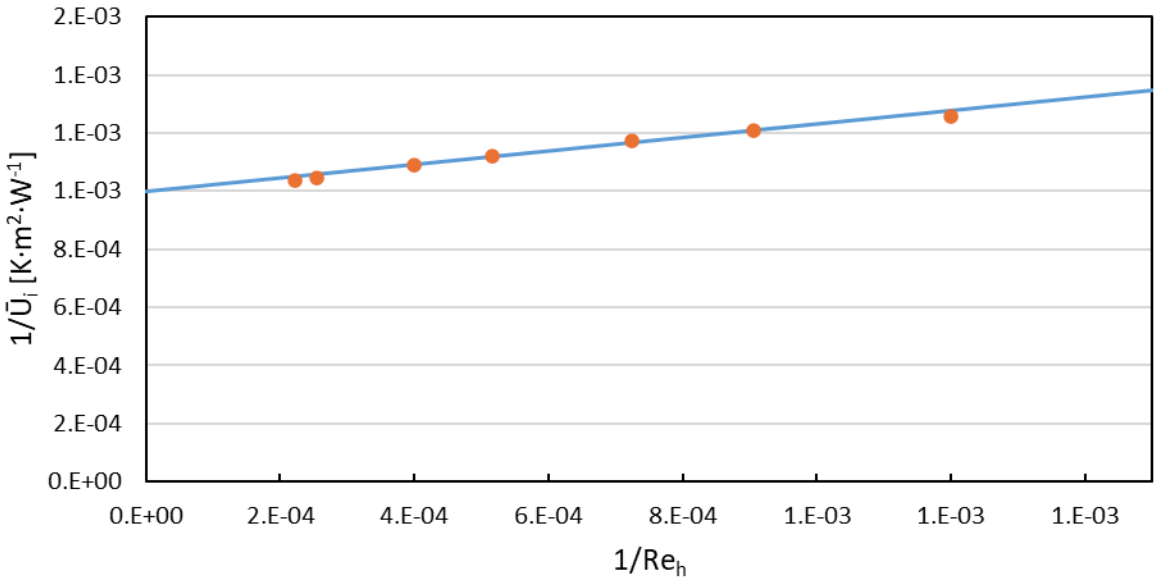

Fig. 2-3: Linear regression for the determination of the inner overall heat transfer coefficient.

2.2.2.3. Residence Time Distribution

In a step change experiment, the cumulative fraction of tracer (F-curve) is obtained from the density measurements of the Coriolis[22,33]. The residence time distribution (E-curve) of the reactor is determined by the differentiation of the F-curve. The relationship between the E-curve and F-curve is demonstrated in equations (12) and (13). The density step change generates either a positive or negative change depending on the tracer's density relative to the original fluid. To convert the raw density measurement of the Coriolis into the F-curve, the densities must be corrected such that they are bounded between zero and unity. This is achieved by removing the baseline measurement and dividing the densities by the maximum recorded value, Eq. (14). In this work, steady-state conditions are achieved when the measured densities are within 0.5% of the maximum recorded value.

$$F(t) = \int_0^t E(t)dt \qquad (12)$$

$$E(t) = \frac{dF(t)}{dt} \qquad (13)$$

$$F(t) = \frac{\rho(t) - \rho_{min}}{\rho_{max}} \qquad (14)$$

The mean residence time, t_m, can be calculated from F(t) via equation (15). The first moment corresponds to the average time a particle spends inside of the reactor. Comparing the space time and the mean residence time to each other some information can be determined from the reactor. If the space time is larger, $t_m < \tau$, then the reactor may experience bypassing or dead spots which reduces the time spent in the reactor compared to the ideal case. On the other hand, if the mean time is greater, $t_m > \tau$, this likely to suggest errors in the data treatment[22,33].

$$t_m = \rho_{max} t_{max} - \int_{t_{min}}^{t_{max}} F(t)dt \qquad (15)$$

The mean residence time is then used to convert the time dimensionless, equation (16). Dimensionless time is preferable as it allows for the residence time distribution to be compared on the same basis regardless of the reactors flow rate. The F-curve is converted from a time basis to dimensionless by adjusting its x-axis, while the E-curve is converted by multiplying it by the mean residence time.

$$\theta = \frac{t}{t_m} \qquad (16)$$

$$E(\theta) = t_m E(t) \qquad (17)$$

At this point, F(θ) can be differentiated to obtain the residence time distribution on a dimensionless time basis. However, due to fluctuations in the density measurements, directly differentiating the F-curve will introduce significant errors to E(θ). Instead, a model is fitted to the experimental F(θ). The F-curve can be modelled with one-parameter or multi-parameter models. One-parameter models such as the tanks-in-series (T-I-S) or the axial dispersion model are applied for their simplicity and practical advantage as their parameter is physically representative. On the other hand, multi-parameter models may achieve better fits, however a drawback is that the parameters may lose physical meaning. Although, the application of statistical distributions can address some of the concerns of multi-parameter models as the parameters are often related to the moments[34].

In this work, the residence time distribution is modelled with the axial dispersion model as it is in good agreement with the experimental data as the skewness of the experimental RTD curve is minor.

The axial dispersion model has specific analytical solutions associated with the boundary conditions of the experimental setup. The two most common boundary conditions for this model are closed-closed or open-open. For a closed-closed boundary condition system, it is assumed that there is no dispersion either upstream and downstream of the reactor[33]. Open-open boundary conditions assume that the fluid experiences dispersion both upstream and downstream of the investigated segment. In this work, open-open boundary conditions are selected based on the tracers' injections, distance from the reactor and the position of the Coriolis at the outlet. The equations associated with both F-curve and E-curve for an open-open boundary conditions are given by equations (18) and (19)[22,33,34].

$$F_{OO}(\theta) = \frac{1}{2}\left(1 + \text{erf}\left(\frac{\theta - 1}{\sqrt{\frac{4}{Pe}}}\right)\right) \qquad (18)$$

$$E_{OO}(\theta) = \frac{1}{\sqrt{\frac{4\pi}{Pe}}}\exp\left(-\frac{(1-\theta)^2}{4/Pe}\right) \qquad (19)$$

The Peclet number, Pe, represents the ratio between the advection transport rate over the diffusive transport rate. The Peclet number is helpful in determining if the reactor operates under plug flow conditions. In practice, plug flow conditions are achieved once the Peclet number is greater than 100 as the impact of axial dispersion, D_a, becomes negligible[22,33,35]. On the other hand, significant axial dispersion is expected as the Peclet number approaches zero.

$$Pe = \frac{advection}{dispersion} = \frac{uL}{D_a} \qquad (20)$$

To optimize the models value of the Peclet number, the residual sum of squares was minimized using a non-linear solver. Once optimized, the second moment of the RTD can be determined with the model. The variance, σ^2, indicates the spread of the residence time distribution. Larger values of the variance indicate broader residence times distributions and thus deviations from plug flow conditions. An important characteristic of the variance is that it increases proportionally with the

length of the investigated segment ($\sigma^2 \propto L$). Thus, it is expected to see an increase in the variance between the inlet and the outlet measurements.

$$\sigma_\theta^2 = \int_0^\infty (\theta - \theta_m)^2 E(\theta) d\theta \qquad (21)$$

Highlighted in the operation conditions, the RTD is taken at both the inlet and the outlet of the reactor allowing to deconvolute the reactor's dispersion from the dispersion added by the upstream piping. The deconvolution is possible as the mean residence time and the variance of the reactor, in a time basis, are additive such that the tracer path can be segmented[22]. Allowing for the reactors contribution to be isolated as shown in equations (22) and (23).

$$t_{m,reactor} = t_{m,outlet} - t_{m,inlet} \qquad (22)$$

$$\sigma^2_{reactor} = \sigma^2_{outlet} - \sigma^2_{inlet} \qquad (23)$$

With the deconvoluted first and second moments of the reactor, the Peclet number of the isolated reactor segment is determined based on the open-open boundary conditions analytical solution. Afterwards, the Peclet number can be used in the axial dispersion model to generate the reactors residence time distribution. This deconvolution approach has a maximum error of 5%, if the Peclet number is greater than 100[22].

$$\frac{\sigma_t^2}{t_m^2} = \frac{2Pe + 8}{Pe^2 + 4Pe + 4} \qquad (24)$$

The experimental trial conditions are listed in Table 2-3. The trial conditions are varied such that the RTD is evaluated from 20 g·min^{-1} to 55 g·min^{-1}, increasing in 5 g·min^{-1} intervals. For each flow rate a repetition is performed to ensure the residence time distribution is robust[36]. This allows for experimental errors to be identified and removed if required. The trials are performed in a manner to always have a positive step change in the density. Thus, the reactor operates with heptane and during the step change the pneumatic valve is actuated to flow THF through the reactor. The space times of the reactor for THF are calculated based on experimental measurements of the reactor volume. This information is useful to evaluate the validity of the experimental mean residence time.

Table 2-3: Experimental conditions for residence time distribution with reactor tube length of 0.48 meters featuring Kenic® static mixers. Low-density fluid is heptane, and the high-density fluid (tracer) is THF.

Trial Identification	Flow rate [g·min^{-1}]	Space Time [s]
7340-25-1 & 7340-25-2	20	8.70
7340-25-3 & 7340-25-4	25	6.96
7340-25-5 & 7340-25-6	30	5.80
7340-25-7 & 7340-25-8	35	4.97
77340-25-9 & 7340-25-10	40	4.35
7340-25-11 & 7340-25-12	45	3.87
7340-25-13 & 7340-25-14	50	3.48
7340-25-15 & 7340-25-16	55	3.16

2.3. Results and Discussion

Maintaining the micromixing conditions of the reactor at different scales is the most important parameter for a type A reaction. Type A reactions have reaction times less than one second and thus are impacted by molecular mass transfer. By ensuring the mixing rate and residence time distribution remains identical at the different scales, the reaction conversion will be maintained[37]. Power dissipation is a valuable scale up factor as it is directly related to the other transport phenomena investigated. The power dissipation is related to frictional pressure drop and friction factors as shown in equation (25). To maintain a constant mixing intensity for different tube diameters, the flow rate of the fluids must be adjusted accordingly. When the flow is fully turbulent such that the friction factor is constant, the relationship between the diameter and the volumetric flow rate for a constant power dissipation is $Q \propto D^{7/3}$[20]. Hence, if the diameter is increased by a factor of 2.5 requiring the flow rate to be increased by a factor of ~ 8.5 for a fully turbulent regime.

$$\varepsilon = \frac{\Delta P \dot{Q}}{\rho V_R} = \frac{f u^3}{2D\phi} = \frac{32 f \dot{Q}^3}{\pi^3 D^7 \phi} \qquad (25)$$

$$\varepsilon \propto D^{-7} \dot{Q}^3$$

Additionally, the temperature of the reactor must be kept within the optimal temperature range to maximize the selectivity and yields of the product. An important parameter to control the temperature in the reactor is the surface-to-volume ratio. When increasing the reactor scale, the surface area of the reactor increases at a slower rate than the reactor volume. This difference in growth impacts the heat transfer capabilities of the reactor as the scale is increased. This is related

to the different scaling factors of the heat of reaction and convective heat transfer. The heat rate from the reaction scales is proportional to the reactor volume, while the convective heat transfer rate is proportional to the surface area. Hence when scaling-up the reactor with constant power dissipation, both the increase in volumetric flow and loss of surface-to-volume ratio increases the heat load that must be removed from the reactor. This relationship is expressed by the fourth Damköhler number[38].

$$Da_{IV} = \frac{r\Delta H_r}{\overline{U}_i a \Delta T_{LMTD}} \qquad (26)$$

To mitigate this effect, solutions have been developed to reduce the heat load on the reactor or increase the heat transfer rate. One such solution is the multi-injection principle where the reaction mass is split and injected along the reactor length. This spreads the heat load of the exothermic reaction along the entire reactor length instead of concentrating it at the inlet. The temperature profile can be adjusted based on the specific reaction kinetics limitations by adjusting the splitting of the reaction mass. Roberge et al. have shown the beneficial impact of the multi-injection approach for type A reactions[18,39]. However, the reactor system in this study is not suitable for the multiple injection principle. The reactor organolithium reaction is unstable and prone to degrade within one second. Furthermore, the reagents used are highly reactive with the products generating additional side-products. Thus, the increased residence time associated with the multiple injections will negatively impact the yield. Alternatively, the inlet temperatures of the reactive and coolant mixture can be reduced to shift the hotspot temperature. This is, however, limited by the equipment operating conditions and the physical properties of the solvents and reactants. Given the properties of reactants and solvents, for the organolithium reaction, the reactor cannot be cooled past -15°C without risking precipitation. Instead, the reactor must be designed in a manner that increases the convective heat transfer. One simple approach is to have parallel reactors (numbering up) allowing the volumetric heat load to be distributed[36].

Proper characterization of the heat transfer and understanding of the scale-up is crucial to optimize the reactor operation, preventing significant losses of the product due to the temperature hotspot. Secondly, the characterization of the heat transfer is important for GMP certification and process robustness. Enabling the modelling and adaptability of the system.

2.3.1. Friction Factor

2.3.1.1. Observations

The frictional pressure drop of the reactor is seen to increase with the hydraulic Reynolds number, Fig. 2-4. This trend is expected as the increase in Reynolds' number is directly related to an increase in fluid velocity when the diameter is constant. As the hydraulic Reynolds number increases, the eddies and vortices found in the tube will intensify increasing the energy dissipated inside the tube, resulting in a higher pressure drop. In a fully turbulent regime, the frictional pressure drop scales to the square of the velocity, while a fully laminar regimes scale linearly with the velocity. Moreover, in the transition regime between laminar and turbulent, the fluid may exhibit a combination of both regimes' behaviors. Hence the generalized friction factor's correlation including both contributions from the laminar and turbulent terms.

The friction factor trends seen in Fig. 2-5 demonstrates the different flow regimes present in the tubes at different hydraulic Reynolds numbers. At low hydraulic Reynolds numbers, less than 500, the friction factor decreases linearly, suggesting a laminar flow regime. While for hydraulic Reynolds numbers above 500, the friction factor begins to flatten as the fluid is entering the transition regime between laminar and turbulent. Above hydraulic Reynolds of 2500, the variation in friction factor is small, indicating that the turbulent regime is largely achieved. Trial 7340-9 does, however, not follow these trends. This deviation is related to the pressure transducer inability to accurately measure the pressure differential at lower Reynolds numbers.

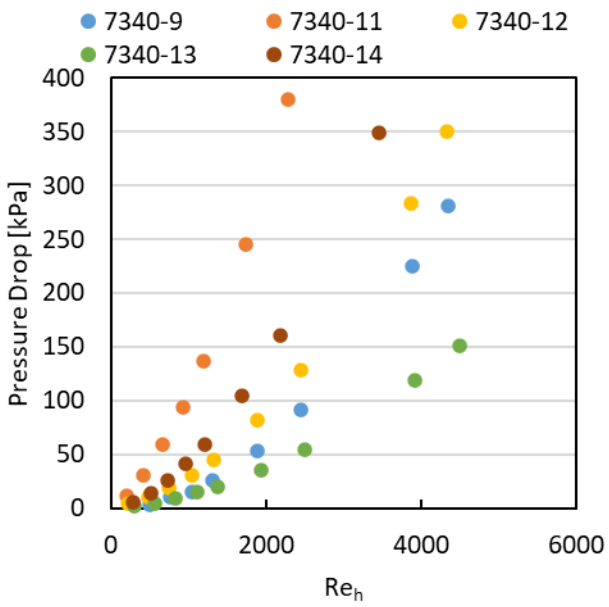

Fig. 2-4: Laboratory frictional pressure drops in relation to the hydraulic Reynolds number.

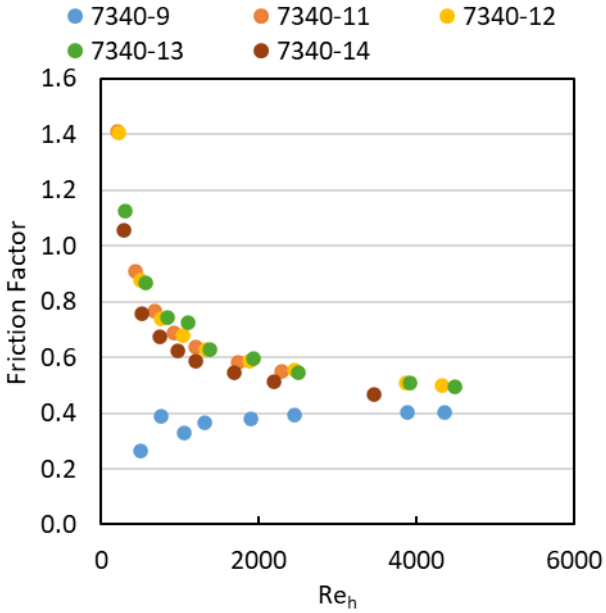

Fig. 2-5: Friction factor in relation to hydraulic Reynolds number.

The impact of tube length on the pressure drop is investigated by plotting ΔP/L as a function of the hydraulic Reynolds number, see Fig. 2-6. Comparing the pressure gradient between the trials with a single tube and three tubes, the pressure gradient is nearly identical for each respective fluid. The lack of variation between the tube length suggests that entrance effects are not prominent and highlights the consistency of the experimental pressure readings between trials.

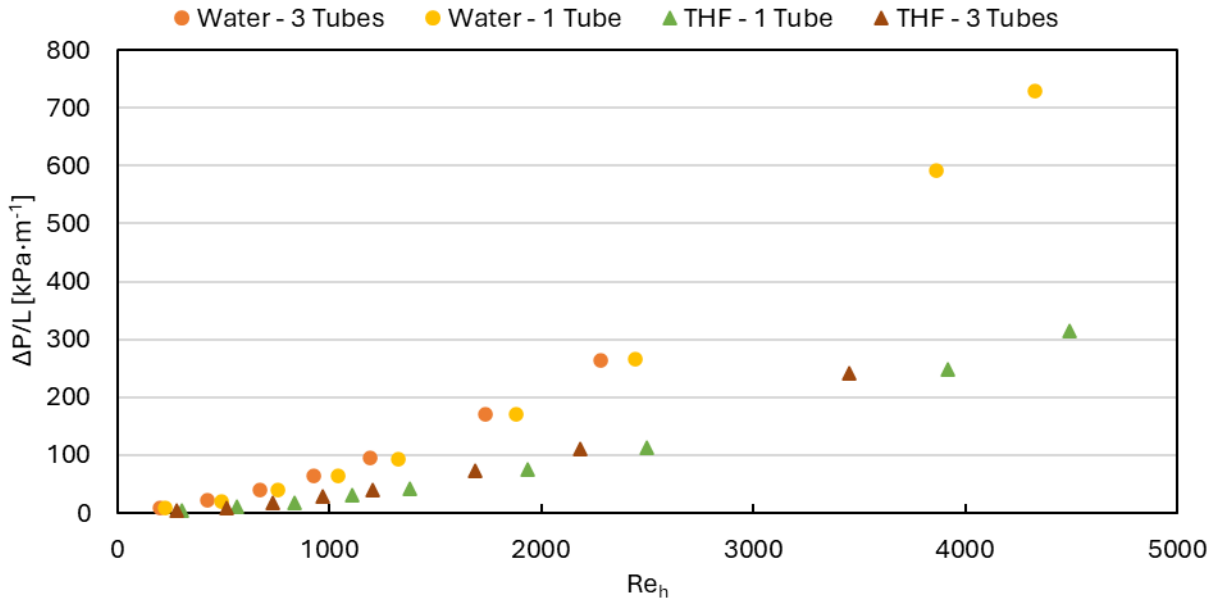

Fig. 2-6: Experimental pressure gradients with respect to the hydraulic Reynolds number. Water indicated by circles and THF indicated by triangles.

The impact of the fluid properties between water and THF is evident in the greater pressure drop measured for the trials with water. This observation aligns with expectations, as water has both a higher density and viscosity compared to THF. In the laminar flow regime, where viscous forces dominate, the pressure drop is strongly influenced by the fluid's viscosity. Since water is more viscous than THF, it experiences greater frictional resistance as it flows, leading to a steeper pressure gradient along the pipe. On the other hand, under turbulent flow conditions, inertial forces govern the pressure drop over viscous forces. Here, the higher density of water will dissipate more energy resulting in larger pressure drops relative to THF.

2.3.1.2. Correlation

The experimental frictional pressure drop is fitted with the pack bed form of the friction factor model, presented in Fig. 2-7 and Fig. 2-8. The two-parameter fit is performed by initially fitting the laminar friction term for Re_h smaller than 500. The turbulent friction factor is fitted afterwards on the remaining measurements. Performing the optimization in this manner improved the agreement of the model and the data. The laminar and turbulent friction factors, for the packed bed structure (c and d), are 191 and 0.45, respectively. The corresponding average absolute relative error (AARE) of the model is 5.05% with a bias factor of 1.03. The consistent fit of the frictional pressure drop and friction factor through the different flow regime supports the generalized friction

factor correlation structure. The correlation is applicable for hydraulic Reynolds numbers of 201 to 4491 with a mixer aspect ratio (Ra) of 1.5, and a tube diameter of 3.05 mm (1.45 mm hydraulic diameter). The friction factor correlation coefficients generated models the Kenics® mixers pressure drop for tube diameters that have not been reported in literature[24,26–29,35,40].

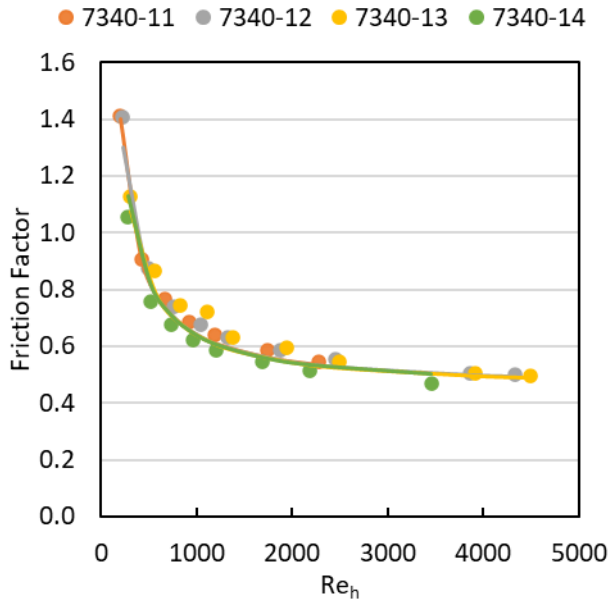

Fig. 2-7: Friction factor model imposed over experimental results. Model added for all experimental trials.

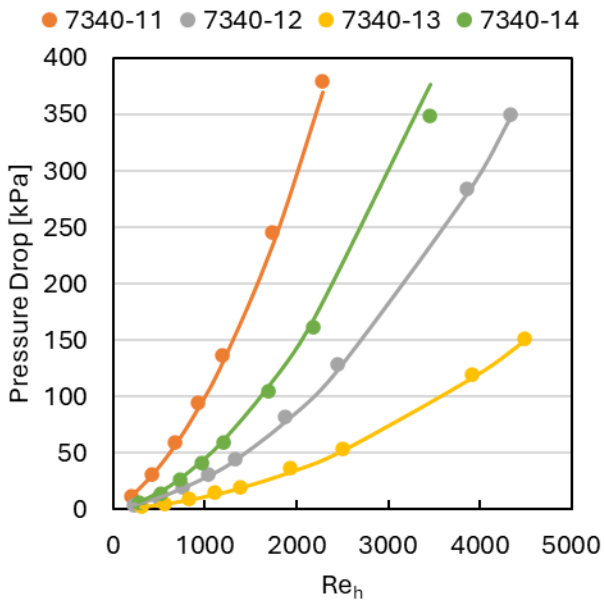

Fig. 2-8: Modelled frictional pressure drop compared with the experimental results.

To better understand the dominant friction factors with respect to the Reynolds number, the relative contributions of the coefficients are plotted, Fig. 2-9. As expected, the laminar friction is dominant at the lower Reynolds ranges. Consistent with earlier findings that the laminar regime is found for Re_h < 500. The rise of the turbulent contribution is seen to slow down past Re_h of 2500. Nevertheless, the laminar contributions converge towards 10% for hydraulic Reynolds numbers in the turbulent regime. However, more data is required to understand this region. A friction factor comparison was performed between the correlation coefficients generated in this work and the literature correlations. The comparison is performed with a chosen hydraulic Reynolds number value of 500 as this corresponds to the beginning of the transition regime. It is found that the coefficients in this work has a friction factor of 0.83 and falls withing the range found by the literature correlations, between 0.42 and 1.56. With Sir and Lecjaks[26] correlation returning the smallest friction factor and Song and Han[29] with the largest.

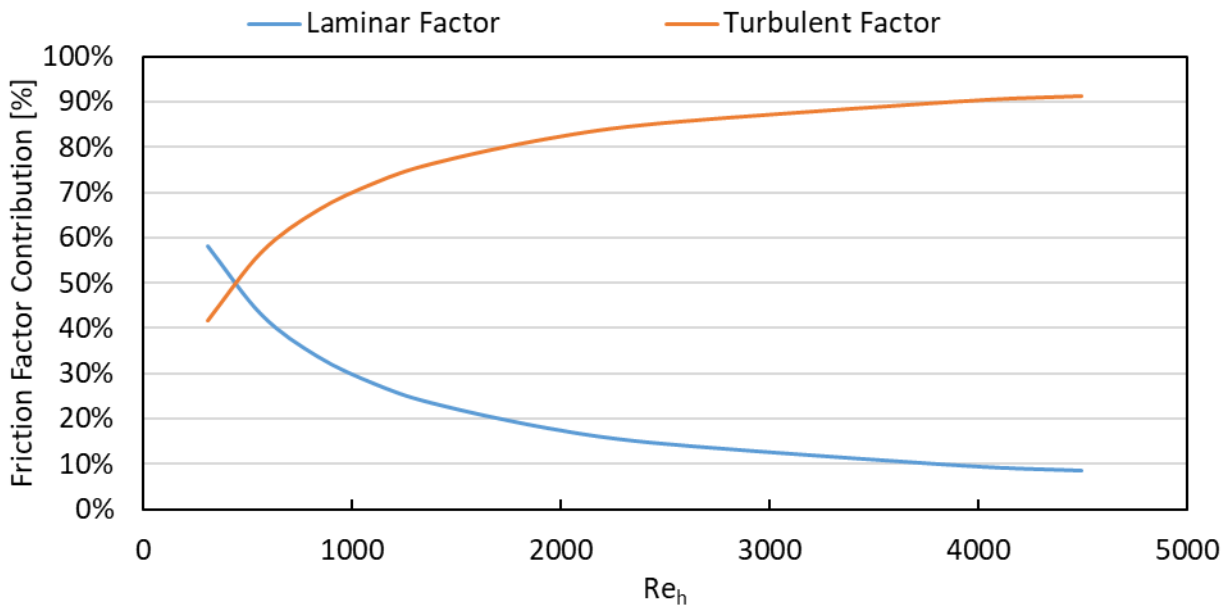

Fig. 2-9: Laminar and turbulent friction factor contribution breakdown with respect to the hydraulic Reynolds number.

2.3.2. Heat Transfer

2.3.2.1. Observations

The experimental trials to investigate heat transfer are identical to the frictional pressure drops and can be found above in Table 2-2. The temperature profile was investigated to determine the average overall heat transfer coefficient to then optimize correlation coefficients for the inner heat transfer coefficient with the Nusselt number. Water and THF were chosen for the heat transfer study to understand the impact of the thermophysical properties and Prandtl number on the heat transfer. The number of tubes increased, from one to three tubes, to determine the entrance effects is significant on the heat transfer. The extracted inner tube Nusselt number and the average overall heat transfer for each trial are displayed in Fig. 2-10 and Fig. 2-11, respectively.

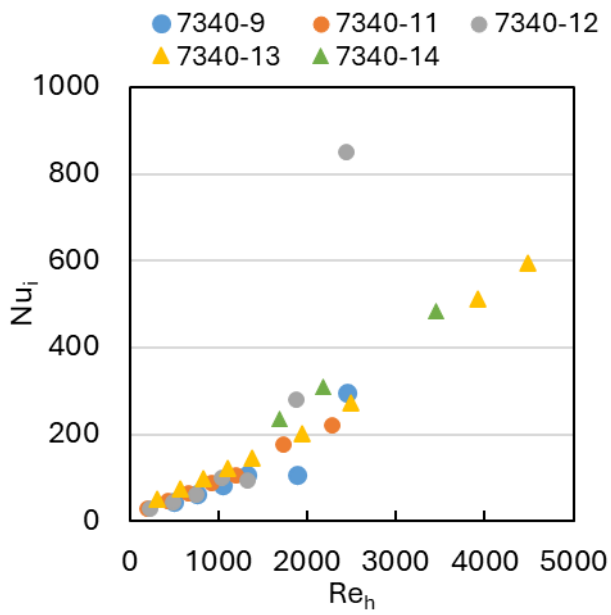

Fig. 2-10: Experimental inner tube Nusselt number for all trials.

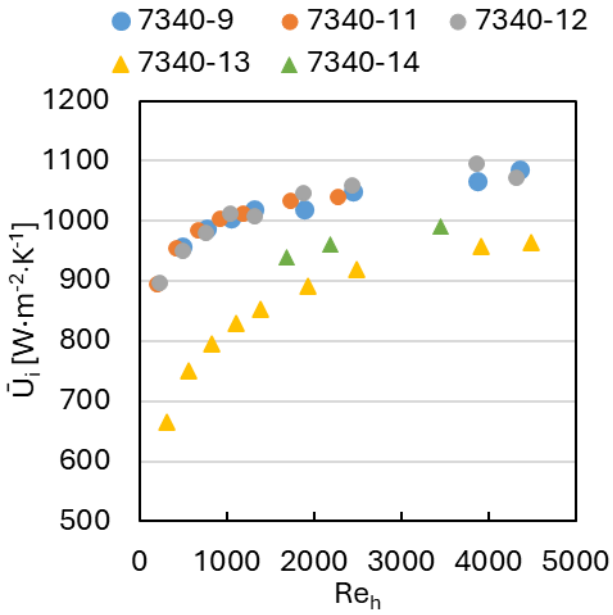

Fig. 2-11: Experimental average overall heat transfer coefficient for all trials.

The inner tube Nusselt number and the averaged overall heat transfer coefficient both demonstrate clear patterns that follow expected trends. Generally, the inner tube Nusselt number increases with the hydraulic Reynolds number and its impact are visible in the overall heat transfer coefficient increases. However, deviations are seen in Fig. 2-10 for the inner tube Nusselt number when hydraulic Reynolds numbers are large. This occurs as the fluid space time through the reactor is small, less than 0.5 seconds, such that the fluid temperature difference between the inlet and the outlet of the reactor are within the thermocouple error. Notably, the last data point of run 7340-12 (see Fig. 2-10) was removed because of this effect. The overall heat transfer coefficient rises quickly at the lower Reynolds number ranges and starts to plateau at high Reynolds numbers, seen when $Re_h > 2300$. The plateauing of the heat transfer coefficient in the system is related to the outer tube heat transfer resistance. The outer tube ethanol flow rate and fluid properties remain constant during the experimentation; thus, keeping the outer tube heat transfer coefficient stable throughout.

At lower hydraulic Reynolds numbers, the inner tube heat transfer is the governing heat transfer resistance of the system. Therefore, when the hydraulic Reynolds number increases so does the averaged overall heat transfer coefficient. This effect is related to the power-law relationship between the Nusselt and Reynolds numbers. The bulk of this effect is seen for hydraulic Reynolds

numbers smaller than 1500. Above hydraulic Reynolds numbers of 1500, the outer heat transfer coefficient begins to govern the overall resistance. Described by the plateau achieved by the averaged overall heat transfer coefficient of ~1050 $W \cdot m^{-2} \cdot K^{-1}$, with water, and ~950 $W \cdot m^{-2} \cdot K^{-1}$, with THF. Increasing the heat transfer medium flow rate would allow the inner tube heat transfer resistance to remain the governing resistance for greater hydraulic Reynolds numbers.

Additionally, the impact of the fluid properties on the overall heat transfer coefficient is observed between the trials with THF (7340-13 and 7340-14) and the trials with water. THF has inferior thermophysical properties due to its lower specific heat capacity, density, thermal conductivity, and viscosity compared to water. The difference in fluid thermal properties translates to a lower heat transfer coefficient for the THF trials compared to water. Nevertheless, the inner tube Nusselt number highlights the consistency of the trends between the heat transfer and the hydraulic Reynolds number.

For trial 7340-14, the overall heat transfer coefficient and Nusselt numbers are not determined for hydraulic Reynolds numbers small than 1500. This is due to the small fluid approach temperature, less than 3°C, obtained experimentally. Resulting in an unreliable $\bar{U}_i$ value as the log-mean temperature difference approaches zero. As such the heat transfer values are significantly impacted by the fluctuations in temperature and the accuracy of the thermocouples. Thus, these data points were omitted from the analysis.

The increase in tube length did not impact the average overall heat transfer coefficient or inner tube Nusselt numbers. This suggests that developing flow region does not significantly impact the overall heat transfer. If this effect was considerable, the Nusselt number would have differed based on the tube length.

2.3.2.2. Correlation

With the experimental inner tube Nusselt numbers, optimized correlation coefficients were determined. The correlation structure applied for the inner tube Nusselt number is that of the modified Gnielinski[12,30]. The modified Gnielinski was selected as the preferred correlation structure as it features the friction factor as one of its parameters. The addition of the friction factor is beneficial due to it accounting for the geometric factor of the static mixers. The robust fit of the friction factor over the entire hydraulic Reynolds number range allows for one set of correlation coefficient to be generated.

The Gnielinski equation inclusion of the friction factor allows the scaling factor to be inherently accounted for in the heat transfer correlation. As the power dissipation is proportional to the friction factor as shown in equation (25). Ensuring the scale effect dependence is characterized by the chosen correlation structure.

$$Nu_i = \frac{(f/8)(Re_h - \beta)Pr}{1 + \gamma(f/8)^{\frac{1}{2}}(Pr^{\frac{2}{3}} - 1)} \qquad (27)$$
$$f = \frac{2\Delta P}{\rho u^2}\left(\frac{d_h}{L}\right) = \frac{191}{Re_h} + 0.45$$

The correlation coefficients of γ and β are found by minimizing the residuals between the experimental data and the model. To prevent a negative Nusselt number, the β-coefficient is limited such that it cannot exceed the smallest experimental hydraulic Reynolds number ($Re_{h,min} < \beta$). The modified Gnielinski characteristic length is the hydraulic diameter of the tubes.

The optimized correlation coefficients are 5.05 and 68.5 for γ and β, respectively. The correlation has an average R^2 value of 0.95, an AARE of 23% and a bias factor of 1.11. The heat transfer correlation maintains an accurate fit for both water and THF heat transfer, Fig. 2-12. The overall heat transfer coefficient is reconstructed using the Nu_i correlation and the β value obtained from the linearization of the overall heat transfer coefficient, Fig. 2-13. This indicates that differences in fluid properties and Prandtl number are well characterized. Furthermore, the robustness of the fit over the entire hydraulic Reynolds range suggests the inclusion of the friction factor sufficiently accounts for the different flow regimes and geometric effects.

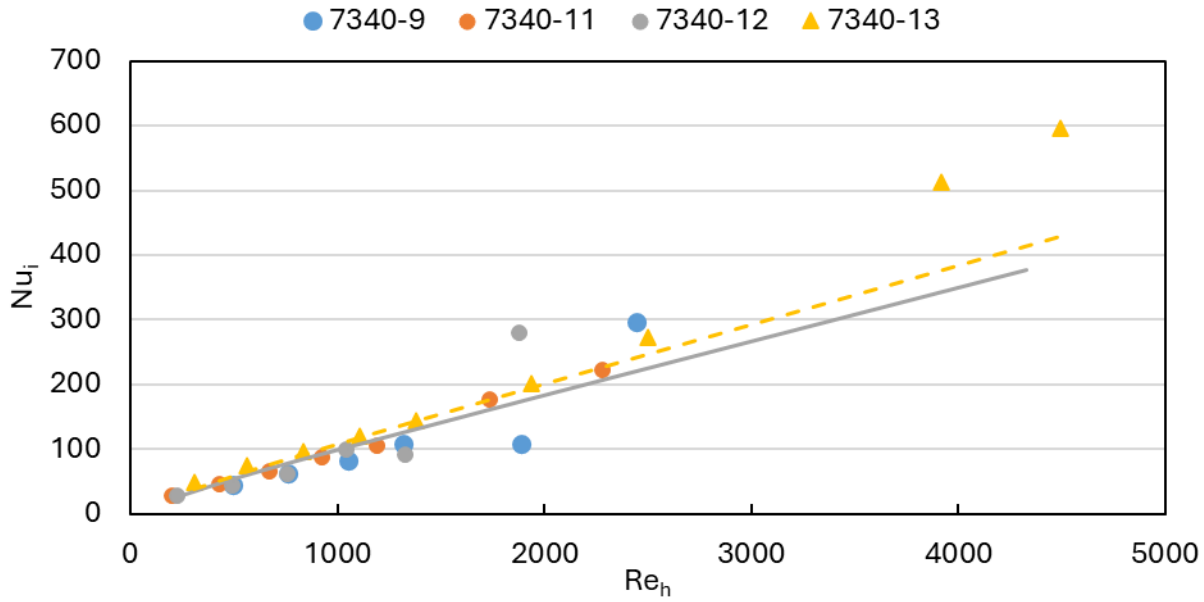

Fig. 2-12: Experimental inner Nusselt numbers compared to Nusselt numbers obtained by modified Gnielinski correlation. Data markers are indicated with circles for water and triangles for THF. THF Nusselt model is represented by the dash line, while water with the full line.

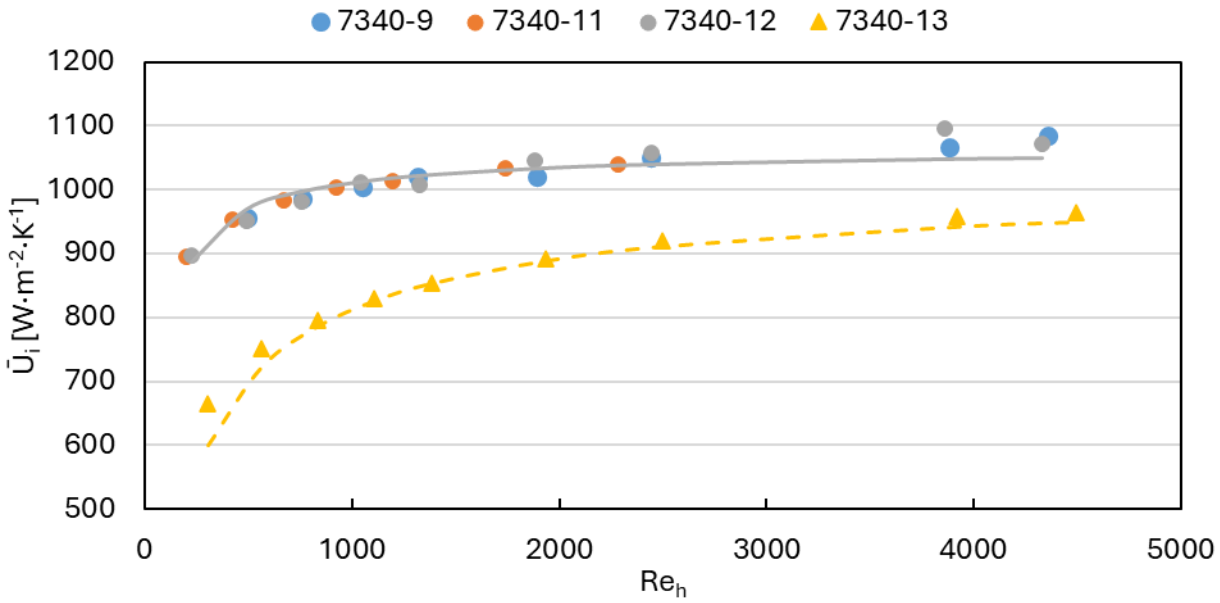

Fig. 2-13: Modelled overall heat transfer obtained by applying the modified Gnielinski correlation for the inner heat transfer coefficient. Data markers are indicated with circles for water and triangles for THF. Dashed line corresponds to THF, and full line to water models.

The average overall heat transfer coefficient profile with respect to the hydraulic Reynolds number can be explained by investigating the relative contributions of the three heat transfer resistances (Fig. 2-14). Heat conduction through the wall offers marginal resistance, that is relatively invariant

with changes in hydraulic Reynolds number. The inner tube heat transfer resistances relative contributions are seen to decrease with the hydraulic Reynolds number. On the other hand, the outer heat transfer coefficient is the governing resistance over the entire Reynolds number, with its contribution never falling below 60%. The outer heat transfer coefficient being the governing resistance does explain the flat overall heat transfer profile obtained experimentally. To alleviate this limitation, increasing the ethanol flow rate is required as this will increase the coefficients value. Although for the trials with THF, the inner tube heat transfer is seen to have an increase contribution compared to water as the poorer thermal properties increased the heat resistance of the inner tube. Nevertheless, the correlation coefficient generated to determine the inner heat transfer coefficient remains valid regardless of the increased resistance of the outer tube heat transfer.

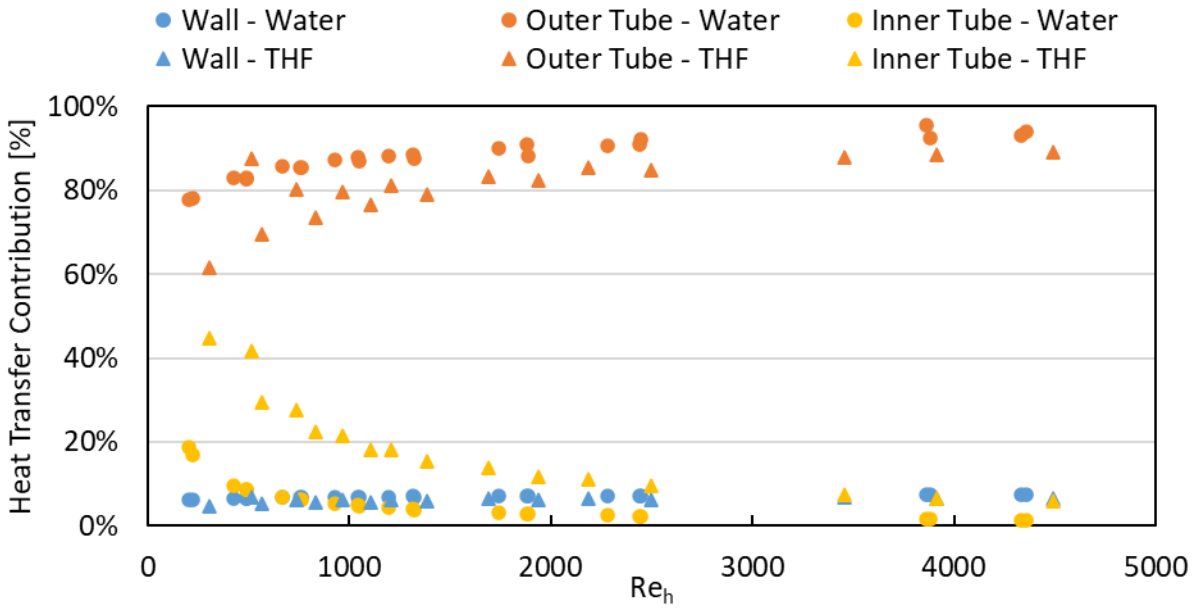

Fig. 2-14: Relative heat transfer resistance contribution for all investigated flow rates and fluids. To distinguish between fluids, data with circles refer to trials with water, and triangles with THF. Wall contributions indicated with blue markers, outer tube orange, and inner tube yellow.

2.3.3. Residence Time Distribution

In Fig. 2-15 and Fig. 2-16, the density step change is seen to increase from the heptane to the THF in a similar manner at the inlet and the outlet of the reactor. This result is crucial for the application of the deconvolution method to determine the mean time and the variance of the reactor vessel. Additionally, the lag time associated with the step change is clearly seen between the two positions.

For the inlet the lag time corresponds to the time required for the THF to reach the reactor inlet, while the outlet includes the residence time of the reactor in its lag time.

Another observation of the raw data, highlighted by the comparison of Fig. 2-15 and Fig. 2-16, is the Coriolis response time. The Coriolis used to measure the density has a response time of 0.5 seconds. This response time can become problematic at the higher flow rates where the space time is roughly six times greater than the instrument's response time. Ideally the response time would be at least 10 times smaller than the investigated phenomena to ensure accuracy[41]. Combined with the residence time distribution of the THF, the response time is insufficient to accurately represent the entire density profile. This is evident for the density profile of the reactor outlet at 50 $g \cdot min^{-1}$, where two observations demonstrate issues with the Coriolis. The first is the sudden and discontinuous increase in the density in one second intervals, and the second is the proximity of the data points recorded at each half second. Importantly, the severity of these jumps in the density measurements is less prominent when the Coriolis is situated at the reactor's inlet.

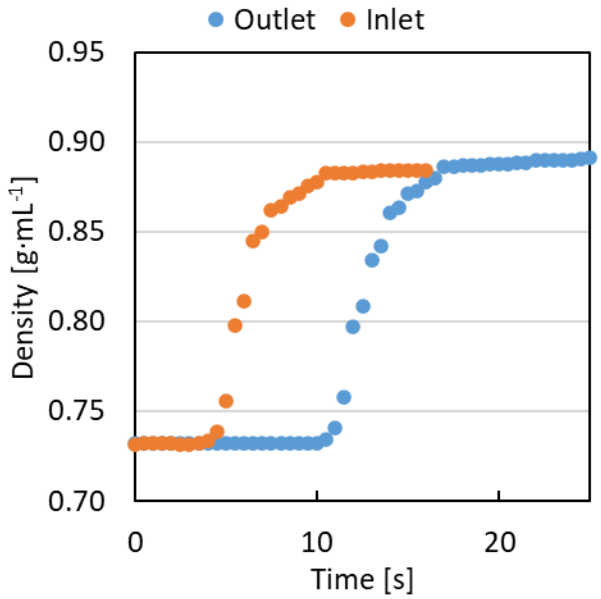

Fig. 2-15: Density step change of trial 7340-25-4, 25 $g \cdot min^{-1}$, for both reactor inlet and outlet.

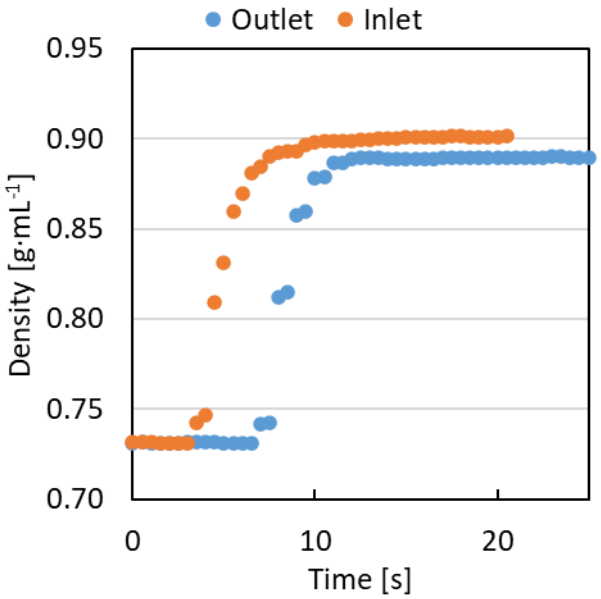

Fig. 2-16: Density step change for trial 7340-25-14, 50 $g \cdot min^{-1}$, for both reactor inlet and outlet.

Nevertheless, the mean residence times obtained from the inlet and outlet density responses are deconvoluted to obtain the reactors mean residence time. This information is used to validate the reactors' mean residence time is within the predicted space times for a given flow rate. The comparison of the reactor mean residence time and the space time expressed as the dimensionless

first moment and compared in Fig. 2-17 with respect to the power dissipation. Power dissipation is chosen as it allows comparison between different reactor scales and is related to the micromixing rate. The reactors dimensionless first moment values, in Fig. 2-17, are taken as the mean of the repetitions with the corresponding standard deviation as the error bar. In the plot, the dimensionless first moment are seen to remain near unity suggesting that the RTD and space time are consistent. The dimensionless mean time does however tend to be above unity which may be an indication that sources of experimental error is impacting the data. These errors can manifest due to differences in the pumps PI control between the trials. The error bars are seen to rise quickly past a power dissipation of 1 $W \cdot kg^{-1}$ as the Coriolis response time is not sufficiently fast.

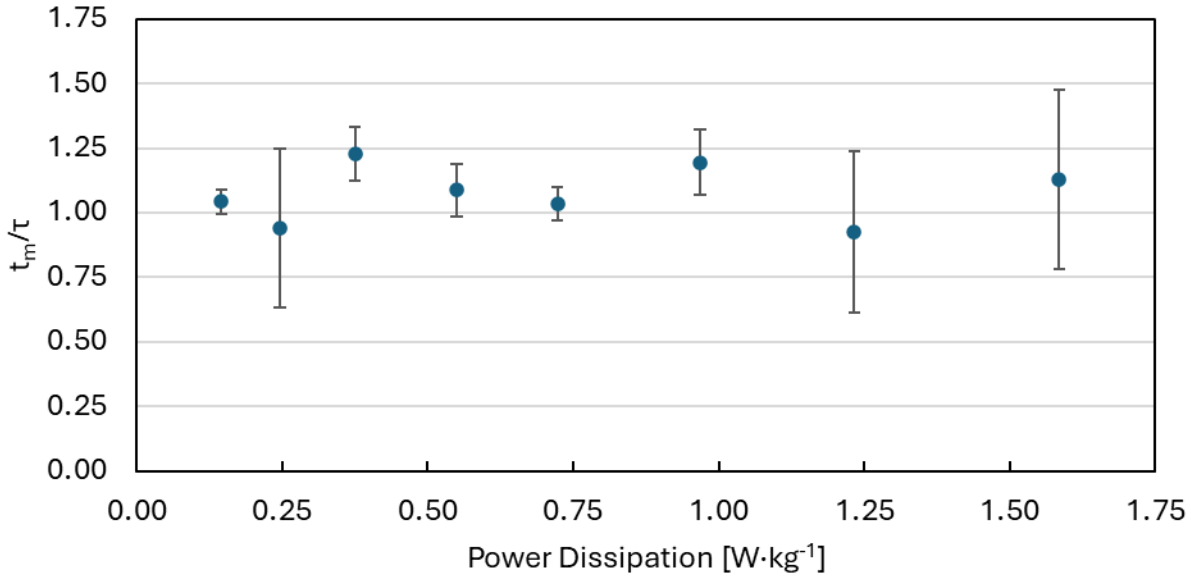

Fig. 2-17: Mean dimensionless first moment (averaged over repeats) for all investigated flow rates, with error bars representing the standard deviation, plotted against power dissipation.

The reactor's mean dimensionless second moment is shown in Fig. 2-18. The dimensionless variance of the reactor, for power dissipation smaller than 0.35 $W \cdot kg^{-1}$, are seen to remain under 0.02. Which corresponds to Peclet numbers greater than 100 and thus is effectively considered plug flow, see Fig. 2-18[22,34]. This is consistent with the shape of the step-change seen in Fig. 2-15 and Fig. 2-16 as the inlet and outlet slope of rise have marginal differences which suggested a near plug flow reactor. However, above a power dissipation of 0.35 $W \cdot kg^{-1}$, the dimensionless variance becomes negative and have significant error bars. This occurs as the outlet variance becomes smaller than the inlet variance. These results are physically impossible as the variance must

increase with length[22,33,35]. Nevertheless, these results support a near plug flow assessment of the reactor as the negative variances are an indication that the small changes in the variance cannot be measured by the precision of the experimental setup

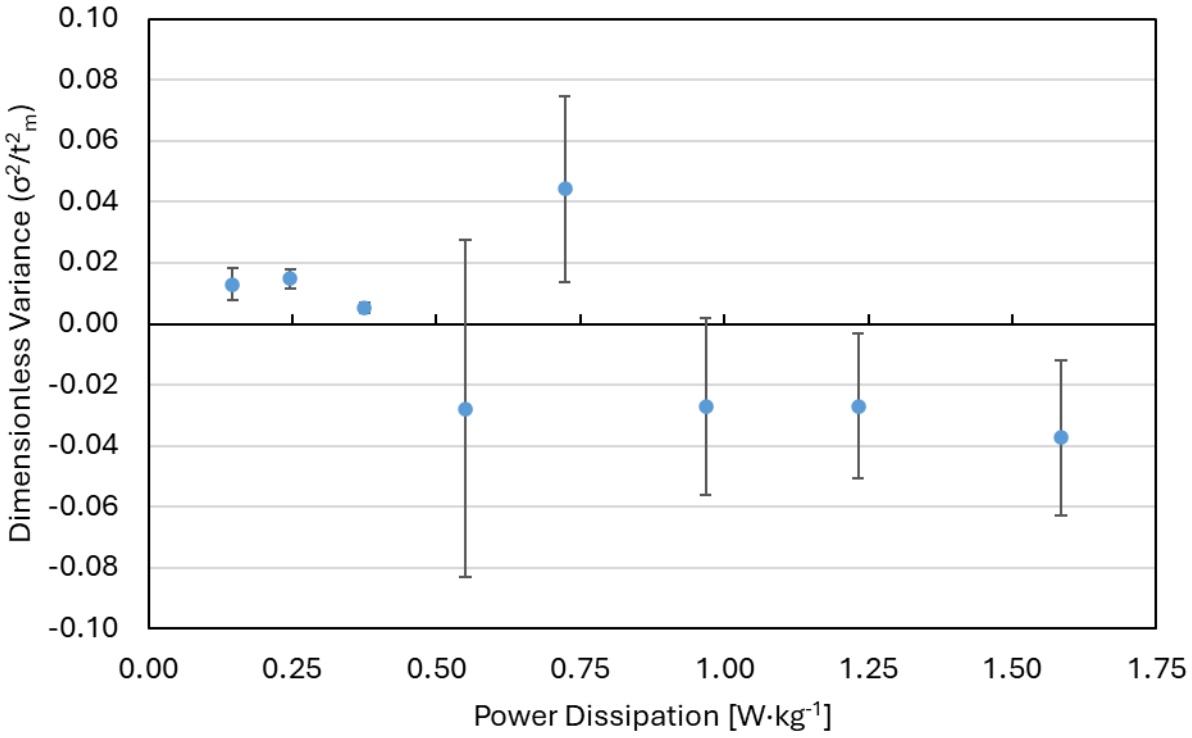

Fig. 2-18: Mean dimensionless variances (averaged over repeats) for all investigated flow rates, with error bars representing standard deviation (n=2), plotted against power dissipation.

The axial dispersion models average absolute relative error for both the inlet and outlet of the reactor is visually represented in Fig. 2-19. The models AARE for all investigated flow rates is 11% with a bias factor of 1.00. Experimental trials with larger AARE generally suffer from lack of fits caused by the skewness of the experimental data which the axial dispersion model cannot address. To better visualize the common fitting issues, the inlet and outlet model for trial 7340-25-4 is shown in Fig. 2-20. In this figure, the axial dispersion model is seen to have increased errors at the tail end of the step-change for the reactor inlet where skewness is present. This issue is persistent at the reactor outlet, however less pronounced. Nevertheless, the impact of skewness is marginal, and the axial dispersion model succeeds in modelling the RTD.

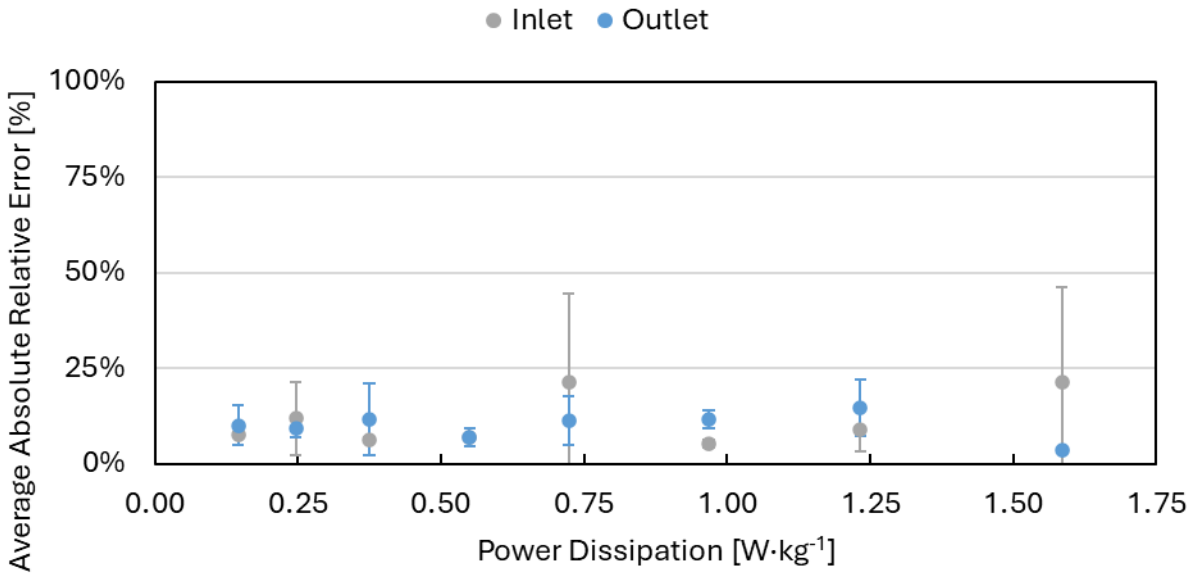

Fig. 2-19: Axial dispersion model mean average absolute relative error (averaged over repeats) for both reactor inlet and outlet at all investigated flow rates, with error bars representing standard deviation (n=2), plotted against power dissipation.

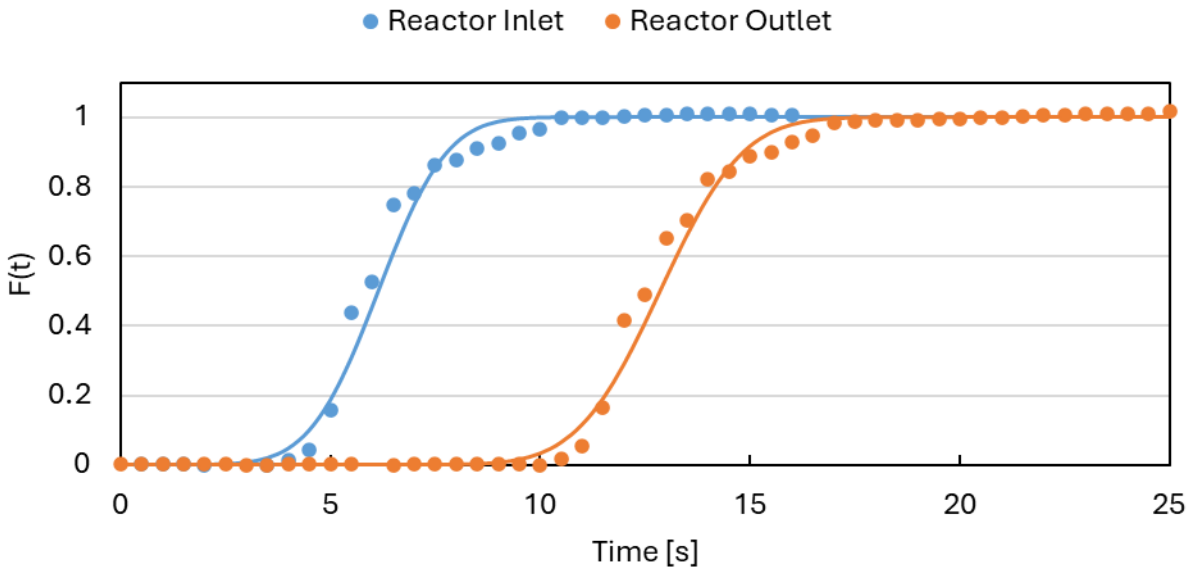

Fig. 2-20: Axial dispersion model imposed on experimental data for trial 7340-25-4 (30 g·min^{-1}) at both reactor inlet and outlet.

2.3.4. Scale-up

As mentioned, power dissipation is the chosen parameter for scaling-up a type A reaction. This ensures the reaction rates are identical by maintaining the micromixing rate at the chosen scale.

One consequence of this approach is the substantial increase in flow rate required to achieve similar mixing conditions. The relationship between these parameters is determined earlier to be $Q \propto D^{7/3}$, when the friction factor is constant. This sharp increase in flow rate is visualized in Fig. 2-21 for four tube diameters, 3.05 mm, 4.57 mm, 6 mm, and 7.75mm. Diameters are selected based on tube size considered for a production S&T reactor.

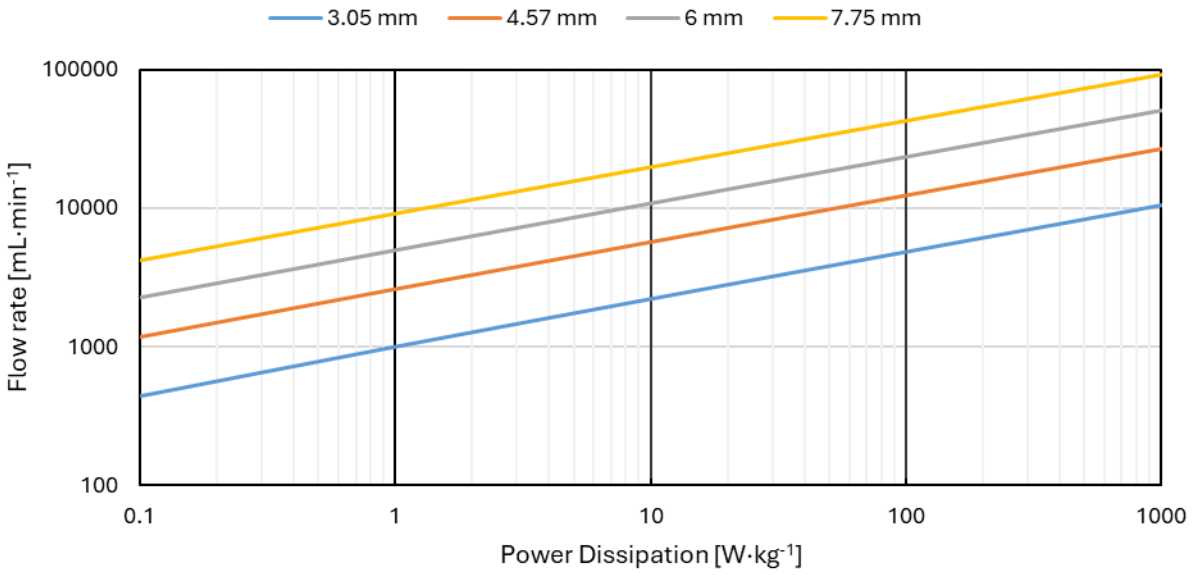

Fig. 2-21: Log-Log flow rate as a function of power dissipation for various tube diameter.

The sharp increase in flow rate can be problematic when selecting equipment at larger scales as these will require additional capital investments and occupy a greater footprint. However, the pressure drop increase caused by the differences in tube diameter can be mitigated by adjusting the reactor length such that the space time remains constant at the different scales. In doing so, this maintains the first Damköhler number (Da_I) constant, seen in equation (28), for a first order reaction. Da_I represents the ratio of the reaction rate to the convective mass transport rate, ensuring similar reaction extents across scales when held constant. The resulting increase in frictional pressure drop with respect to the volumetric flow rate is seen in Fig. 2-22. For a given flow rate, the frictional pressure drop remains similar regardless of the tube diameters. The slight differences seen in the frictional pressure drop are caused by minor changes in the friction factor due to differences in the hydraulic Reynolds numbers.

$$Da_I = k\tau \qquad (28)$$

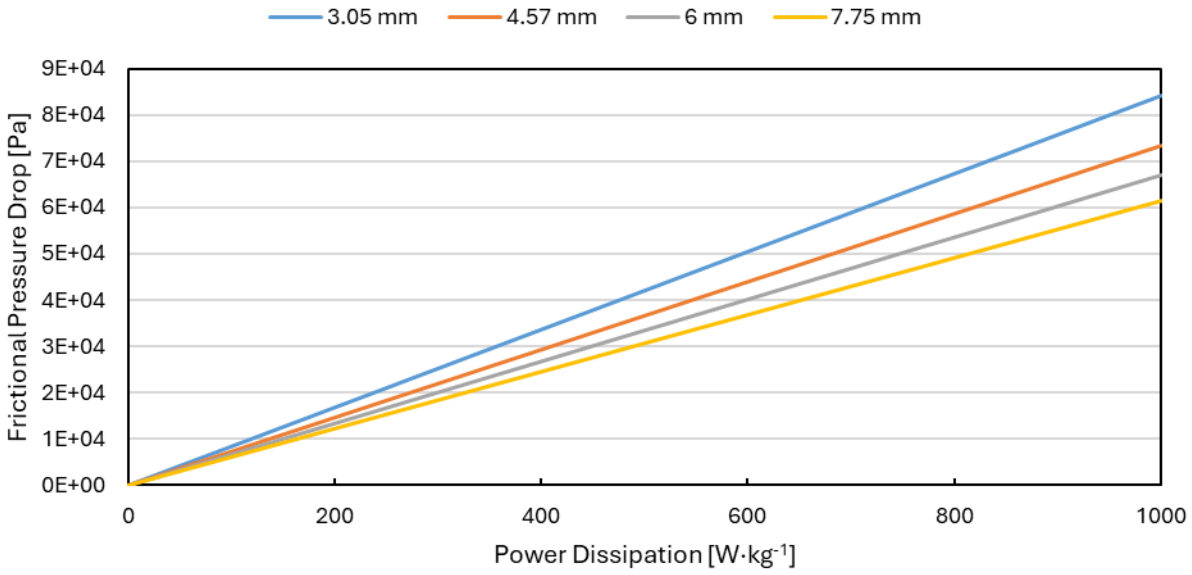

Fig. 2-22: Frictional pressure drop as a function of power dissipation for various tube diameters.

The heat transfer concerns in reactor scale-up are centered on the inherent scaling mismatch between the heat generated by the reaction and convective heat transfer. While the heat generated by the reaction scales volumetrically, the convective heat transfer is limited by surface area. This disparity is aggravated as larger tube diameters reduce the surface-to-volume ratio, intensifying the heat load that must be removed by cooling systems. Mielke et al.[12] has shown that the inner heat transfer coefficient values will remain similar at different hydraulic diameters during scale-up, $\frac{h_{i,2}}{h_{i,1}} \approx 1$. This result is corroborated in Fig. 2-23 where the tube diameters and length are adjusted to maintain a constant ε and Da_I with respect to the volumetric flow rate. The associated power-law regression generated demonstrates that the inner heat transfer coefficients ratio is proportional to $\dot{Q}^{0.1462}$. Thus, if h_i is rate governing, then the overall heat transfer coefficient will hardly vary with scale.

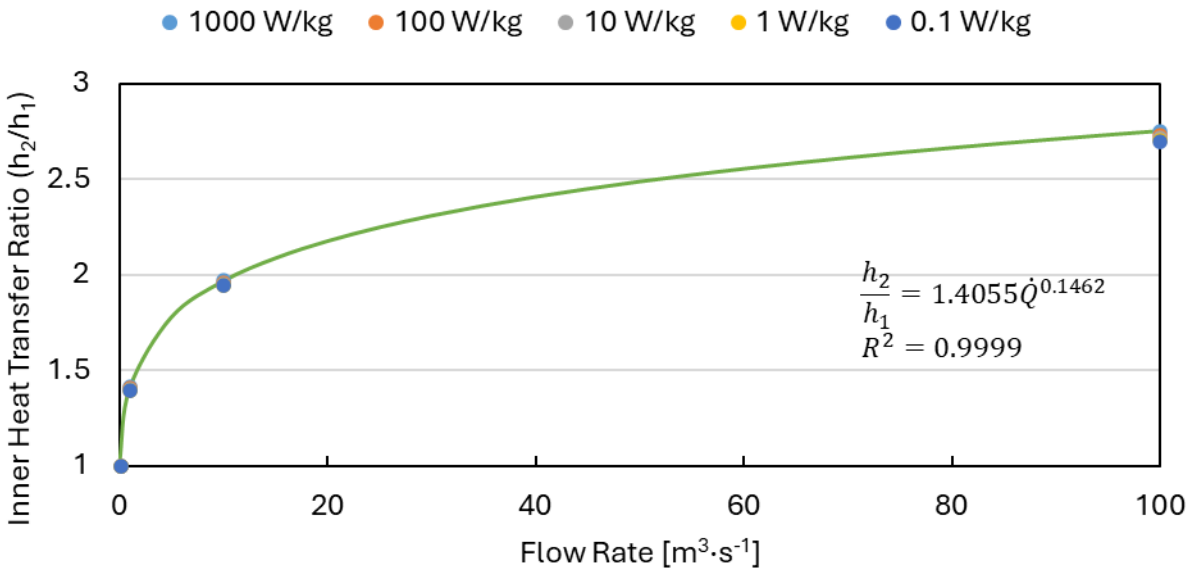

Fig. 2-23: Inner heat transfer coefficient ratio with respect to volumetric flow rate for various diameters. Power-law regression fitted over data points and equation displayed.

Nevertheless, the heat load that must be removed from the reactor increases with respect to the reactor's scale. This is demonstrated in Fig. 2-24 and Fig. 2-25 as the inner heat transfer coefficient value is greater for larger tube scales when increasing the power dissipation. However, this trend flips when the volumetric impact is accounted, see Fig. 2-25. This contrast clearly demonstrates the scale-up concerns associated with the surface-to-volume ratio. Hence at larger scales, the temperature hotspots may impact negatively the production by decreasing product selectivity due to side-reactions. All the while, the increased reactor volumes increase the safety risks associated with thermal runaways, general process operations, and operator safety. To mitigate these risks, larger scale systems need to address the convective heat transfer limitations by adjusting the reactor technology, or its operation conditions. The multi-injection principal is one such solution if reaction conditions are permissible. Otherwise, the reactors can be scale-up to a permissible scale and operated as a system of parallel reactors (numbering up)[36]. The number of reactors in parallel is chosen such that each reactor has sufficient convective cooling to operate safely and achieve production targets.

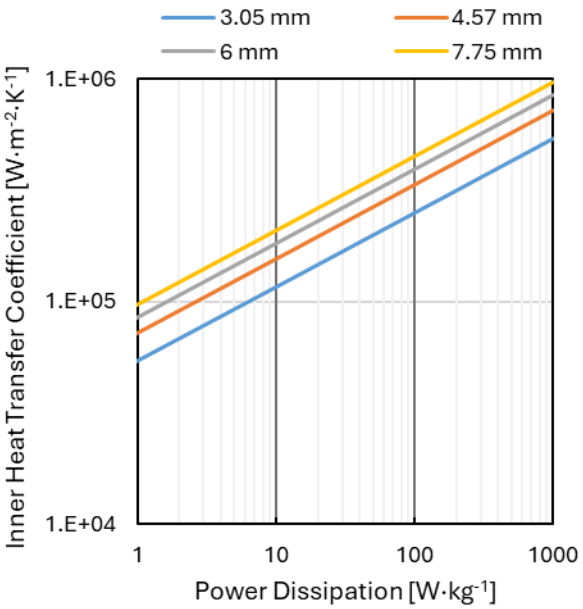

Fig. 2-24: Log-Log inner heat transfer coefficient as a function power dissipation for various investigated tube diameters.

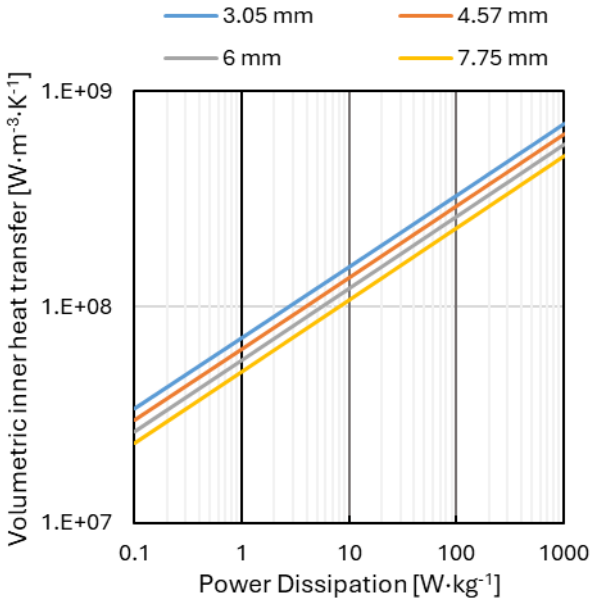

Fig. 2-25: Log-log volumetric inner heat transfer coefficient as a function of power dissipation for various investigated tube diameters.

2.4. Conclusions

The transport phenomena of a continuous shell and tube reactor applied for the GMP production of a pharmaceutical APIs was performed. The frictional pressure drop and inner Nusselt number correlations coefficients generated are valid for tube diameters not previously reported in literature. All correlations coefficients have demonstrated accurate fits of the experimental data at various fluid flow conditions and physical properties, Reynolds number, and fluid thermal properties, Prandtl number. The associated average absolute relative errors for the friction factor and inner Nusselt number correlations are 5% and 23%, respectively. It found that the fluid operated under laminar conditions when the hydraulic diameter Reynolds numbers are below 500 and reached a fully turbulent regime for hydraulic Reynolds number greater than 2500.

The residence time distribution characterization found that the reactor operates effectively in plug flow conditions with the Peclet number meeting the minimum threshold of 100. During the deconvolution, issues were encountered when the power dissipation went above 0.35 $W \cdot kg^{-1}$ as the second moment became negative. This error was identified and associated with the Coriolis response time of 0.5 second which failed to accurately measure the tracer's step change at high flow rates. Regardless, the experimental results suggest that near plug flow conditions are

maintained at larger power dissipation as both inlet and outlet tracer response have similar trends. The sensitivity of the RTD, within the measurement error, to the Peclet number is marginal when Pe > 100, as such no trend was established between Pe and power dissipation over the range investigated. In addition, the axial dispersion model accurately fitted the RTD with an average absolute relative error of 11%.

Power dissipation scale-up demonstrates the relationship between the frictional pressure drop and heat transfer transport phenomena. The frictional pressure drop was seen to increase with power dissipation in a consistent manner with the tube diameters when the first Damköhler number is kept constant by adjusting the reactor's length. Maintaining a constant Da_I ensures the reactions extents are similar at increased scales. While the inner heat transfer coefficient ratio was shown to remain nearly identical when the power dissipation is kept constant by adjusting the tube diameter and flow rates. Nevertheless, the loss surface-to-volume with scale-up was identified by contrasting the inner heat transfer coefficient with the volumetric inner heat transfer coefficient. This comparison demonstrated the clear loss in convective heat transfer due to increasing tube diameters. Solutions to alleviate these concerns are proposed, such as the multi-injection principle to fractionate the heat load along the reactor length and numbering up the process by having multiple reactors in parallel.

3. Continuous Flow Microstructure Static Mixer Calorimeter Heat of Reaction Determination for Mixing Limiting Reactions

3.1. Introduction

In recent years, the formation of active pharmaceutical ingredients (APIs) has seen a transition from conventional batch processes towards continuous flow chemistry processes. This transition from batch to continuous processes has been favored as continuous processes can be miniaturized and intensified to increase throughput and product quality[3]. Flow chemistry reactors are often miniaturized to micro- or milli-scales for process development. The reduction in reactor volume is beneficial to the reactor's safety by decreasing safety concerns associated with large reactant volumes, such as runaway reactions or explosions[5,6]. In addition, the smaller reactor scales improve the temperature control of the reactor[7,8]. Continuous flow reactors are beneficial to the pharmaceutical industry as they can perform reactions that are ill-suited or impossible to produce in a batch process[10]. Specifically for reactions characterized by fast reaction times, unstable products prone to degradation or side-reactions, and thermal runaway concerns.

To scale the production of an API from research and development (R&D) to production scales, the reaction calorimetry must be understood. The reaction calorimetry is conventionally found in batch processes, for example Mettler Toledo® RC1mx unit[42,43]. However, batchwise processes may not be applicable when reaction time scales are smaller than the mass transport, or when precise control over the reaction temperatures are required[10]. Few continuous calorimeters have been reported in literature and fewer are available for commercial applications[19,44–52]. Moreover, the specific techniques applied to get the heat of reaction do differ. An approach is heat flux measurements from the thermoelectric effect, Seebeck effect, are applied to convert the temperature differences into an electric potential[47–49,51,52]. Otherwise, temperature measurements are taken with thermocouples, or infrared cameras, to generate energy balances[12,19,44,45,53]. In this work, the calorimeter is designed for local temperature measurements with inline thermocouples. This approach has been shown to have comparable accuracy with industrial batchwise calorimetry equipment for selective reactions[44].

Of importance is to characterize the thermal hotspot in micro- or milli-scale continuous reactors for highly exothermic reactions. The broadness and magnitude of the hotspot corresponds to the reaction time and exothermicity of the reaction, respectively. Increasing the scale of the reactor,

the cooling potential of the reactor diminishes relative to the energy added by the exothermic reaction. A consequence of the reaction exothermicity scaling with the volume, while the cooling rate scales with the surface area. This worsens the broadness of the hotspot impacting negatively the yield and selectivity of the reaction. Understanding the characteristics of the hotspot while obtaining the heat of reaction is another benefit to continuous calorimeters for process scale-up.

In this work, the heat of reaction for the synthesis of lithium diisopropylamine (LDA) from n-butyllithium (nBuLi) and diisopropylamine (DIPA) is investigated and reported in a continuous calorimeter. The LDA synthesis is an organolithium reaction that behaves as a type A reaction as classified by Roberge et al.[16] for flow chemistry applications. The heat of reaction is calculated by solving the energy and the associated species balances differential equations with a MATLAB® simulation. The LDA synthesis kinetic model is examined under mixing limiting conditions. The heat of reaction is evaluated at different flow rates and overall reaction kinetic constants. Lastly, the heat of reaction from the MATLAB® simulation is compared with heat of reaction obtained by a discrete heat model outlined in Steinemann et al.[19]. The limitations and advantages of both methods are discussed.

3.2. Equipment

The continuous calorimeter experimental setup is shown in Fig. 3-1. The jacketed tubular reactor has a length of 500 mm, inner diameter of 7.8 mm, and an outer diameter of 10 mm. The interstitial volume of the calorimeter is 16.5 mL, corresponding to a void fraction of 69%. Static mixers and an axial temperature sensor are found in the inner tube of the calorimeter. Two static mixers are used in the reactor, one promoting intense mixing between the two fluids injections (CSE-X/4), and a second type for increased heat transfer (CSE-X/6). The CSE-X/4 mixer has an inner diameter of 4.6 mm and spans 23.5 mm, while the CSE-X/6 has an inner diameter of 7.8 mm and spans the remainder of the reactor. The axial temperature sensor has a diameter of 1.6 mm with 10 thermocouples (Class 1, type K). The thermocouples have an accuracy of ±1.5°C, and are spaced by 51 mm. The first temperature measurement is taken 34 mm in the reactor. The associated cooling jacket of the calorimeter has an inner diameter of 13 mm, flowing in a co-current configuration. Ethanol is the selected cooling fluid with a setpoint temperature of -35°C. The ethanol temperature is recorded at the inlet and the outlet of the jacket with thermocouples. The ethanol flow rate is kept constant at 310.1 $kg \cdot h^{-1}$. The cooling jacket inlet is positioned, 18.5 mm,

from the reactor inlet. The two feeds are flow rates are controlled with a dosing module, assembled of Ismatec® Reglo-Z gear pumps and a Bronkhorst Coriolis mass flow controller. The dosing modules are interfaced with a HiTec Zang for data acquisition. Where the HiTec Zang controls the dosing module by adjusting the pumps amperage, via PI controller, based on the Coriolis flow rate measurements. Both nBuLi and DIPA feeds are pre-cooled from room temperature in an Ehrfeld Mikrotecknik A6 FlowPlate® Rack before reaching the calorimeter's inlet. The FlowPlate® Rack features five plates totaling 32.12 mL, two plates with mixers and serpentine channels and the remaining featuring only serpentine channels. The temperature of both feeds is recorded using thermocouples, Pt100 Class A sensor, at the calorimeters entrance. The ethanol is cooled with a Huber CC905 chiller. The instruments data is recorded in 5 second intervals with the HiTec Zang.

The total feed flow rate in the calorimeter is investigated at four set points: 45.7 $mL \cdot min^{-1}$, 69.4 $mL \cdot min^{-1}$, 104.1 $mL \cdot min^{-1}$, and 142.8 $mL \cdot min^{-1}$. Feed-1 is composed of 23 wt.% nBuLi stabilized in hexanes. Feed-2 mixture is 19.2 wt.% DIPA with the remainder as THF. The proportion of each feed is controlled to have a molar equivalence of 1.08 $\frac{mol_{nBuLi}}{mol_{DIPA}}$. This molar equivalence corresponds to a flow rate ratio of 1:1.6 for Feed-1:Feed-2.

The tubing connections of the system are constructed in stainless steel (AISI 316) with a nominal diameter of 3.175 mm. The continuous calorimeter and inner tube equipment, static mixer and thermocouples, are constructed in stainless steel (AISI 316). The thermal conductivity of the stainless steel is taken as 15 $W \cdot m^{-1} \cdot K^{-1}$[54].

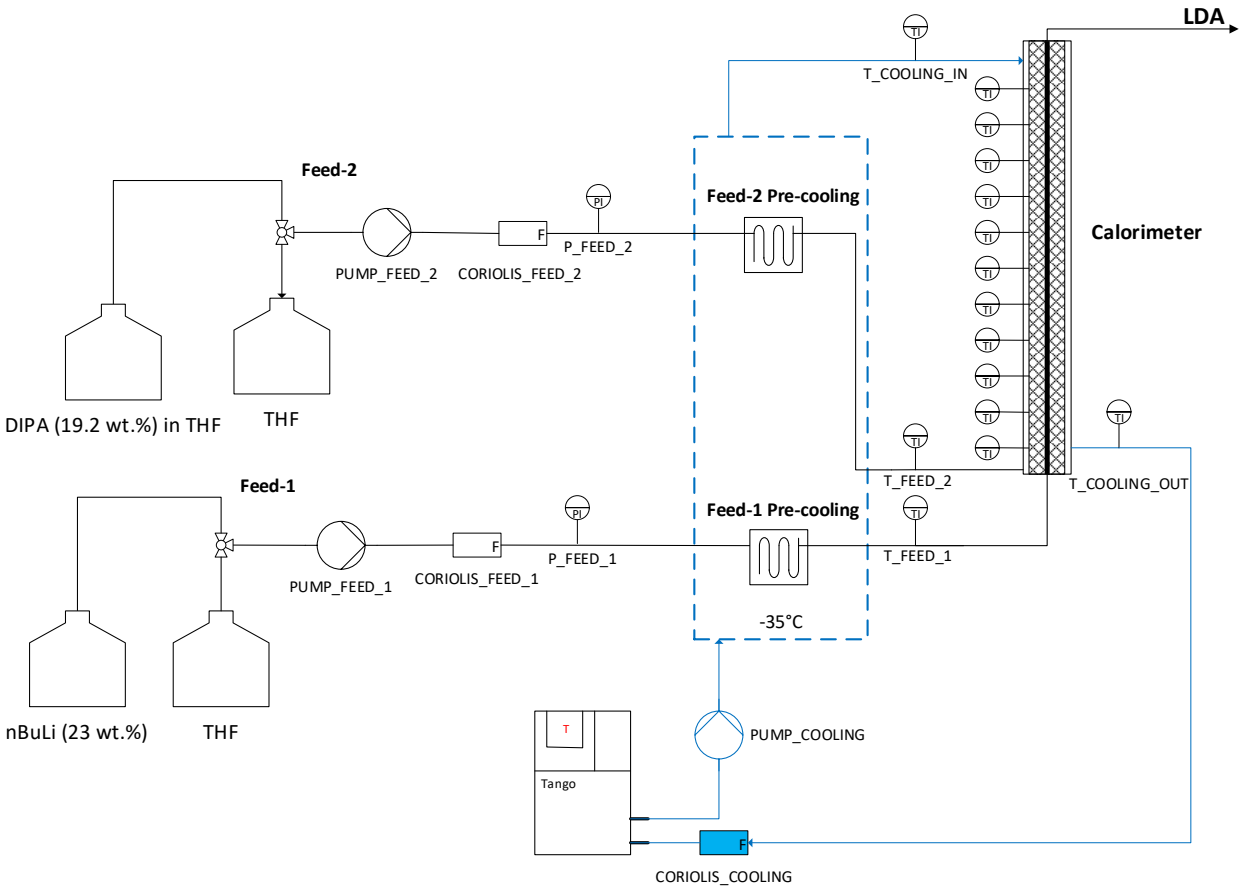

Fig. 3-1: Continuous calorimeter process flow diagram.

3.2.1. Chemical Reaction

The synthesis of the lithium diisopropylaminde (LDA) is performed by reacting n-butyllithium (nBuLi) and diisopropylamine (DIPA).

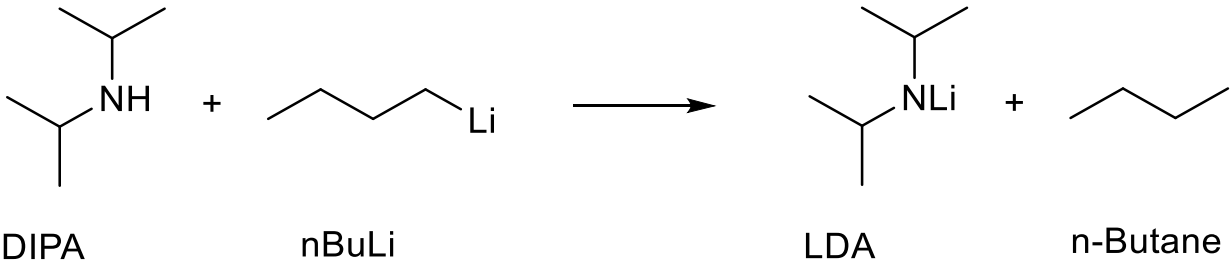

Organolithium reactions are highly reactive[8,55] and described as a type A reaction by the classification outlined in Roberge et al.[16]. Type A reactions, or fast reactions, have reaction times less than one second and are thus controlled by the micro-mixing conditions of the reactor rather than the reaction kinetics. The type A behavior of the reaction mandates the use of the CSE-X/4

static mixers, as their high mixing intensity ensures rapid homogenization and minimizes mass transfer limitations.

The fast reaction times and high mixing intensity generated from the static mixers ensures the use of a pseudo-first order overall reaction kinetic model for the LDA reaction. Unfortunately, the specific kinetic information concerning the activation energy and pre-exponential constant are unknown for the LDA reaction. However, the overall reaction rate is parametrically varied to ensure mixing rate is governing.

3.2.2. Experimental Procedure

The calorimeter operation begins by pre-cooling the reactor by recirculating the cooling fluid until the setpoint temperature is achieved. Once pre-cooled, the reactants are fed in the reactor and the thermocouple temperature are monitored until steady state is reached. At steady state, the temperatures are recorded for the heat of reaction analysis. Measurements are taken at 5 second interval with the HiTec Zang. The reactant flow rate is then modified to the next setpoint. This process is repeated until all flow rates are investigated.

3.3. Energy Balance

The energy balance in the liquid phase of the continuous flow calorimeter is one-dimensional in the axial direction, assuming steady-state conditions. The energy balance accounts for the thermal conductivity of the fluid in the axial direction. The fluid's thermal conductivity is included in the energy balance as the sharp increase in temperature at the inlet of the reactor is expected to promote heat conductivity downstream. The convective cooling between the jacket fluid and the inner tube is included in the energy balance. The overall heat transfer coefficient in the energy balance is normalized on the inner tube area. Radial temperature profiles in the system are not accounted for as the presence of static mixers is assumed sufficient to have a homogenous cross-section. The energy balance is calculated with superficial conditions as the complex geometry of the mixers and central temperature probe are difficult to simulate accurately without multidimensional and local conservation equations solved via CFD software's.

$$\mathrm{k_f}\frac{\partial^2 T}{\partial z^2} - \frac{\dot{m}C_p}{A_c}\frac{\partial T}{\partial z} + U_i a(T_\infty - T) + H_{rx} r_i = 0 \qquad (29)$$

To determine the heat of reaction from the energy balance, the associated species balance of the reactive species is required. The species balance follows an ideal plug flow reactor equation. The

reaction rate is assumed to follow a pseudo-first order kinetic model due to mixing limiting conditions[56].

$$\frac{\partial F_i}{A_C \partial z} = r_i \tag{30}$$

$$r_i = -k_o C_i \tag{31}$$

To solve the system of ODEs, four parameters must be determined in the energy and species balances. These parameters are the fluids thermal conductivity (k_f), the overall heat transfer coefficient (U_i), the overall reaction rate (k_o), and the heat of reaction (H_{rx}). These parameters are determined by splitting the calorimeter into two segments: a reactive zone and a cooling zone. The position of the segments is based on the length required for the LDA reaction to achieve completion.

The overall reaction rate constant is expressed as a system of resistance between mass transfer and the reaction kinetics. For type A reactions, the mixing times, will be greater than the reaction times. Thus, it is assumed, and confirmed experimentally, that the intrinsic reaction rate is much greater than the mixing rate ($k_r >> k_{mix}$). The overall rate constant can be approximated as being associated only with the mixing rate of the system (Eq. (33))[45].

$$\frac{1}{k_o} \approx \frac{1}{k_r} + \frac{1}{k_{mix}} \tag{32}$$

$$\frac{1}{k_o} \approx \frac{1}{k_{mix}}, Mixing\ limited \tag{33}$$

Experimental mixing times were found with a Villermaux-Dushman reaction in the calorimeter. The mixing times were found to be less than < 0.25 seconds at the lowest flow rate investigated (45.7 mL·min^{-1}). This corresponds to a mixing rate constant of roughly 4 s^{-1} for the smallest flow rate, increasing to around 20 s^{-1} for 140.1 mL·min^{-1}.

The reactor length required for the reaction to achieve completion, conversion of 99.9%, was calculated by solving equations (30) and (31), which yields equation (34) and represents the first Damköhler number for a first-order reaction[22]. For the given flow conditions in the calorimeter, the reaction space times ranged from 1.1 to 0.2 seconds from the lowest to highest flow rate. These space times correspond to a length of 16 to 25 millimeters, respectively. The reaction completion is thus achieved before the first inline temperature measurement. The calorimeters segments are

such that the cooling segment begins after the first axial temperature measurement in the reactor, see Fig. 3-2.

$$Da_I = k_o\tau = \ln\left(\frac{C_{A0}}{C_A}\right) = \ln\left(\frac{1}{1-X}\right) \qquad (34)$$

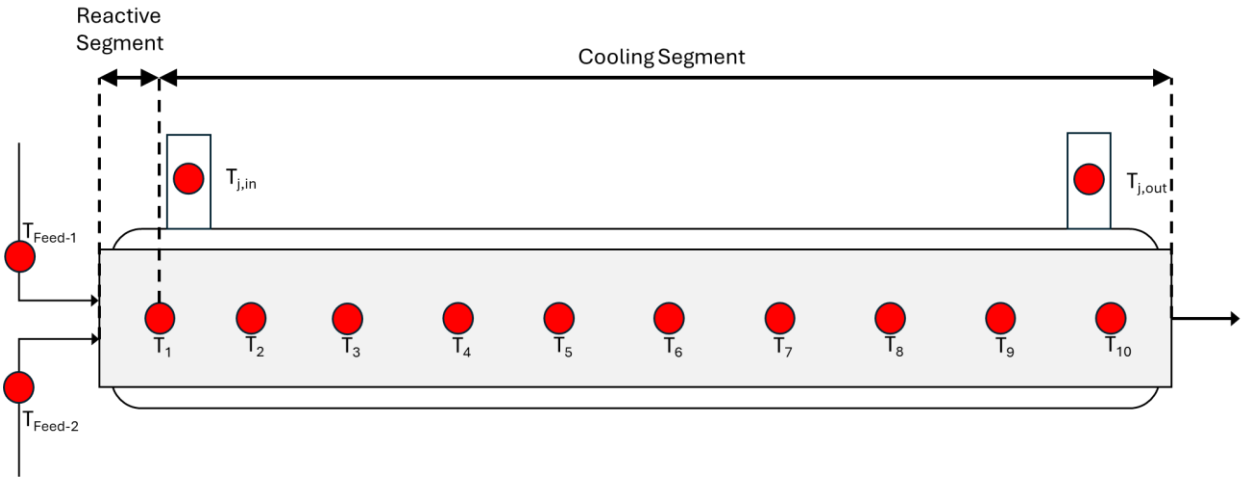

Fig. 3-2: Continuous calorimeter inline temperature measurement with reactive and cooling segments identified, not at scale.

3.3.1. Simulation

To determine the heat of reaction from the energy balance, a MATLAB® simulation was applied. The simulation solves the system of ODEs using an *ODE15s* numerical approach. The heat of reaction is determined by performing a best fit of the axial temperature profile with experimental data. The optimization is performed using an *fminsearch* function in MATLAB® with the objective function minimizing the residual sum of squares between the temperature at the measurement locations. Alternatively, the area under the curve can be matched between the experimental and the simulation for the optimization. However, this has been shown by Steinemann et al.[19] to be inaccurate if the peak temperature is not measured properly in the experimental data.

The MATLAB® simulation takes into consideration the temperature dependence of the fluid physical properties (viscosity, specific heat capacity, and thermal conductivity). Since the reaction mixtures physical properties were not experimentally obtained, the properties are estimated with correlation generated from the Design Institute for Physical Properties (DIPPR) of the American Institute of Chemical Engineers (AIChE)[57]. The physical properties of the reaction mixture are taken as THF as it accounts for 51 wt.% of the mixture. The temperature dependence of density was not accounted to maintain the mass continuity of the simulation.

3.4. Results and Discussion

3.4.1. Fluid Thermal Conductivity

The thermal conductivity of the fluid and the overall heat transfer coefficient are determined in the non-reactive segment of the reactor. The energy balance is thus adjusted to remove the heat of reaction term, and the species balances are not simulated. The fluid thermal conductivity and the overall heat transfer coefficient are determined by performing a two-parameter fit through the experimental data. The parameter fit is performed using a MATLAB® simulation, where both parameters are fitted by minimizing the difference between the model and the experimental data temperature measurements. To simplify the computation, an average value for the overall heat transfer coefficient is used in the cooling section rather than finding local values. The fluid thermal conductivity is initialized as 15 $W \cdot m^{-1} \cdot K^{-1}$ and the overall heat transfer coefficient at 500 $W \cdot m^{-2} \cdot K^{-1}$.

The results of the fit found that the calorimeter cooling is governed by the convective heat transfer and that the conductive heat transfer of the fluid is negligible. The best fit of thermal conductivity for each investigated flow rate was set to zero by the algorithm. While the fitted average heat transfer coefficients were found to be between 500 and 550 $W \cdot m^{-2} \cdot K^{-1}$, see Table 3-1. The fitted parameters further support the presence of static mixers in the calorimeter tubes to promote both homogenous mixing and convective heat transfer.

Nevertheless, the fluid thermal conductivity was modified manually, with the average-overall heat transfer coefficient found by the optimization (Table 3-1), to investigate the impacts it may have on the thermal profile. Validating the previous methodology. The thermal conductivity was varied between 0 to 15 $W \cdot m^{-1} \cdot K^{-1}$for these tests. The upper bound value corresponds to the stainless steel's thermal conductivity acting as the theoretical maximum for the system. The temperature profile for a given flow rate of 142.8 $mL \cdot min^{-1}$ while the fluid thermal conductivity is adjusted between zero and 15 $W \cdot m^{-1} \cdot K^{-1}$ is plotted in Fig. 3-3 to highlight the negligible impact it has on the temperature. The minimal change in the temperature profile maintains that the dominant cooling mechanism of the calorimeter is the convective heat transfer.

Table 3-1: Calorimeter fluid thermal conductivity and average-overall heat transfer coefficient parameters best fit for all investigated flow rates.

Flow rate [mL·min^{-1}]	Fluid thermal conductivity [W·m^{-1}·K^{-1}]	Average-overall heat transfer coefficient [W·m^{-2}·K^{-1}]
45.7	0	499
69.4	0	512
104.1	0	534
142.8	0	547

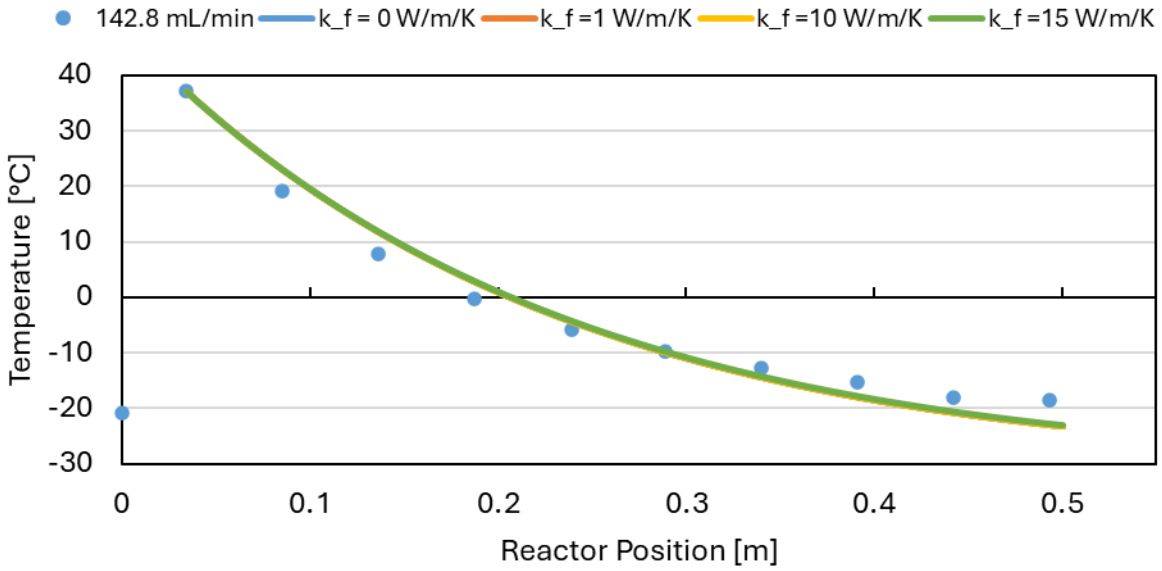

Fig. 3-3: Calorimeter axial temperature profile of the reactors cooling segment with respect to reactor position for a flow rate of 142.8 mL·min^{-1}. Fluid thermal conductivity is varied between zero and 15 W·m^{-1}·K^{-1}. Temperature profiles coincide across all thermal conductivities.

3.4.2. Overall Heat Transfer Coefficient

Local measurements of the overall heat transfer coefficients are required to accurately represent the temperature profile and determine a representative heat of reaction. One approach is to take the non-reactive segments temperature profile and extract the local overall heat transfer coefficient. The local heat transfer coefficients obtained by this method will correspond to the middle point position between the temperature sensors. The local overall heat transfer coefficient is calculated by adjusting Eq. (35). The heat transfer area is taken as the inner tube surface area.

$$U_i(x) = \frac{\dot{m} C_p (T_{i+1} - T_i)}{A_s \Delta T_{LMTD}} \qquad (36)$$

$$\Delta T_{LTMD} = \frac{\left(T_i - T_{j,i}\right) - \left(T_{i+1} - T_{j+1}\right)}{\ln\left(\frac{T_i - T_{j,i}}{T_{i+1} - T_{j+1}}\right)} \qquad (37)$$

The resulting local overall heat transfer coefficient profile generated from the experimental data decreases sharply with the reactor position, Fig. 3-4. This suggests that potentially one or more of the heat transfer resistances in the overall heat transfer coefficient decreases with the reactor length. The heat transfer resistances in the reactor are associated with the outer and inner fluids heat transfer coefficients, and the tube wall resistance between the jacket and the inner tube. Additionally, the conductive resistances of the solid phase: static mixer blades, thermocouple sleeve wall, and thermocouple internals may not be negligible; thus, contributing to the sharp decline in overall heat transfer coefficient. Since the outer fluid and inner fluid flow conditions are relatively constant past the reactor's inlet, the change in the local overall heat transfer must be related to the conductive resistances of the thermocouple rod and static mixers. If this is true, this may explain the near constant local overall heat transfer coefficients found past 0.3 meters in the reactor. As one must assume that the conductive contributions of the solid phase become negligible past this distance. Furthermore, in Fig. 3-4 local $U_i(x)$ values are not reported for thermocouple positioned past 0.35 meters as the temperature difference between measurement are too small to be measured accurately by the Pt100 thermocouples.

However, the lack of geometric information on the thermocouple's construction and complex geometries of the static mixers prevent this analysis from being completed. Nevertheless, to investigate this complex geometry, a three-dimensional multiphase energy balance applied on both solid and fluid phases are required. This analysis would require the application of computational fluid dynamic (CFD) software to solve local conservation equations in both phases. In lieu, an alternative methodology must be applied to address the decline in the heat transfer coefficients.

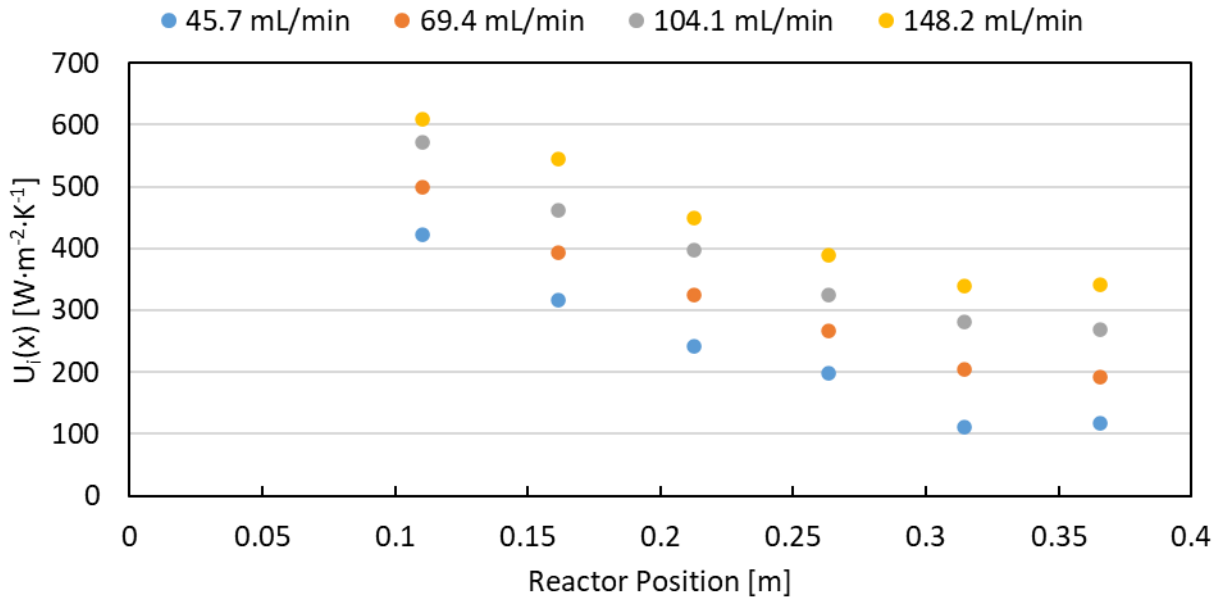

Fig. 3-4: Experimental local overall heat transfer coefficient extracted from the experimental temperature profile of all flow rates in the non-reactive segment of the calorimeter. Reactor position is taken as the middle point between individual thermocouple measurements.

3.4.2.1. Empirical Approach

One alternative is to determine the local overall heat transfer coefficient based on empirical correlations. For this approach, the local overall heat transfer coefficient is assumed to include the convective resistances from the inner tube, outer tube, and conductive wall resistance. Omitting the additional conductive resistances associated with the static mixer and thermocouple rod. The convective inner and outer heat transfer are determined with Nusselt number correlations, while the wall resistance is based on the wall thickness of the tube wall. With these an estimate of the local overall heat transfer coefficeint can be determined.

Based on this methodology, the local overall heat transfer coefficients were determined in partership with Fluitec. Fluitec, the manufacturer of the calorimeter and static mixers, have investigated and determined the overall heat transfer coefficient with empirical correlations in past publications[44,45]. Having extensively characterized the calorimeter, Fluitec has generated proprietary empirical correlations for the calorimeter to predict the overall heat transfer coefficient.

$$U_i = \frac{1}{\frac{1}{h_i} + \frac{A_i}{A_o h_o} + A_i R_{wall}} \qquad (38)$$

The corresponding local overall heat transfer coefficient from Fluitec maintains the general trend seen in the experimental data, however, the decrease in local values with position is less severe, see Fig. 3-5. To interpolate the local overall heat transfer coefficients, for simulation purposes, a power-law regression was generated for each flow rate following the structure outlined in Eq (39). Nevertheless, the heat transfer estimates at the inlet of the reactor are bound to be innaccurate from the developping flow profile, caused by the fluids injection and the differences in mixer geometry and diameters.

$$U(x) = Ax^b \tag{39}$$

Additionally, the thermal profile is expected to be developping as the cooling jacket fluid inlet is offset by 18.5 mm from the inner fluids inlet. As a result, the thermal conditions from the reactor's inlet to the first axial temperature measurement will differ from the remainder of the reactor. As mentionned earlier, a three-dimensional multiphase CFD simulation on the energy balance would be required to solve the local conservation equations to model the complexities associated to the heat transfer at the reactors inlet. To mediate this issue, the local overall heat transfer coefficient is maintained constant from the inlet to the first estimate of the local value. This assumption is likely to over-estimates the local overall heat transfer coefficient, but minimizies the extrapolation errors that are associated with predicting the inlet segment.

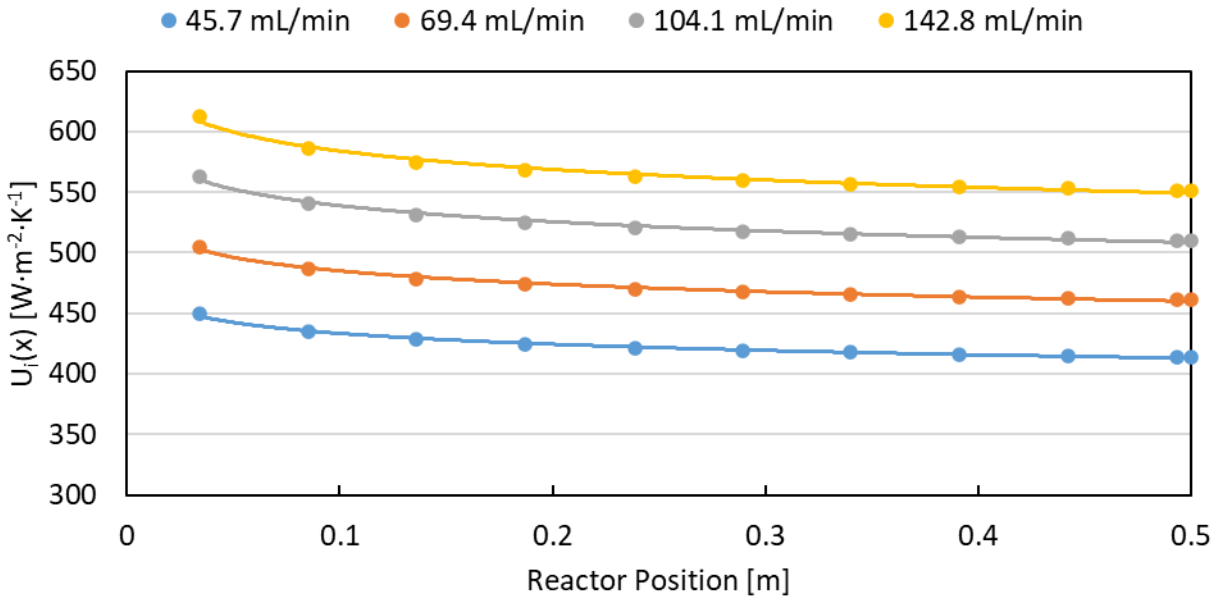

Fig. 3-5: Local overall heat transfer coefficients reported by Fluitec with generated power-law regressions models.

The power-law regression generated on the local overall heat transfer coefficient reported by Fluitec has a fit where the coefficient of determination (R^2) is above 0.99 for all flow rates investigated. The power-law regression coefficients are listed below in Table 3-2. For the determination of the LDA heat of reaction, the local overall heat transfer coefficient power-law regression generated from Fluitec's report values will be utilized.

Table 3-2: Power-law regression of local overall heat transfer coefficients for investigated flow rates.

Flow rate [mL·min^{-1}]	A-coefficient	*b*-coefficient
45.7	404.32	-0.030
69.4	449.48	-0.033
104.1	495.87	-0.036
142.8	534.74	-0.038

3.4.3. LDA Heat of Reaction

In the reactive segment, two parameters must be determined to solve the energy balance, the overall reaction rate (k_o) and the heat of reaction (H_{rx}). To obtain the heat of reaction, a sensitivity analysis between the two parameters was performed by altering the value of the overall reaction rate. The lower and upper bounds for the sensitivity analysis are set as the mixing rate estimates and a characteristic mixing rate of 250 s^{-1}, respectively. The upper bound value is selected such as that second Damköhler number (Da_{II}), see Eq. (40), remains governed by the mixing rate ($Da_{II} > 1$)[38] with an assume reaction rate (k_r) of 1000 s^{-1}[44]. The estimated mixing rates from the Villermaux-Dushman reaction were selected as the lower bound as preliminary simulation showed that decreasing the overall reaction rate past these values would yield in poor simulation results. Notably, the simulated temperature profile would fail to match the initial temperature rise of the experimental data as the reaction rate becomes governing for these conditions.

$$Da_{II} = \frac{k_r}{k_{mix}} \tag{40}$$

The corresponding sensitivity analysis of the overall reaction rate found that past a critical reaction rate, the best fitted heat of reaction remained constant, Fig. 3-6. This effect is caused by the overall reaction times being sufficiently fast to achieve the adiabatic temperature rise. The opposite phenomenon is obtained near the estimated mixing times. In this case, the convective heat transfer can reduce the reaction mixtures temperature before the reaction achieves completion.

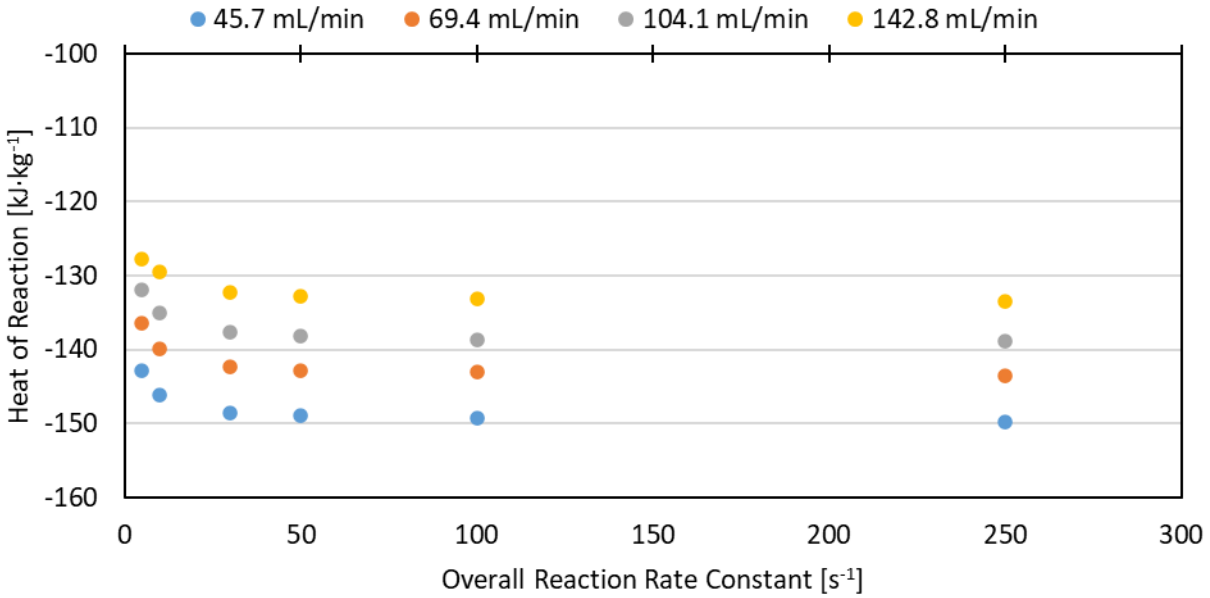

Fig. 3-6: Heat of reaction best fit with respect to the overall reaction rate for all flow rates investigated.

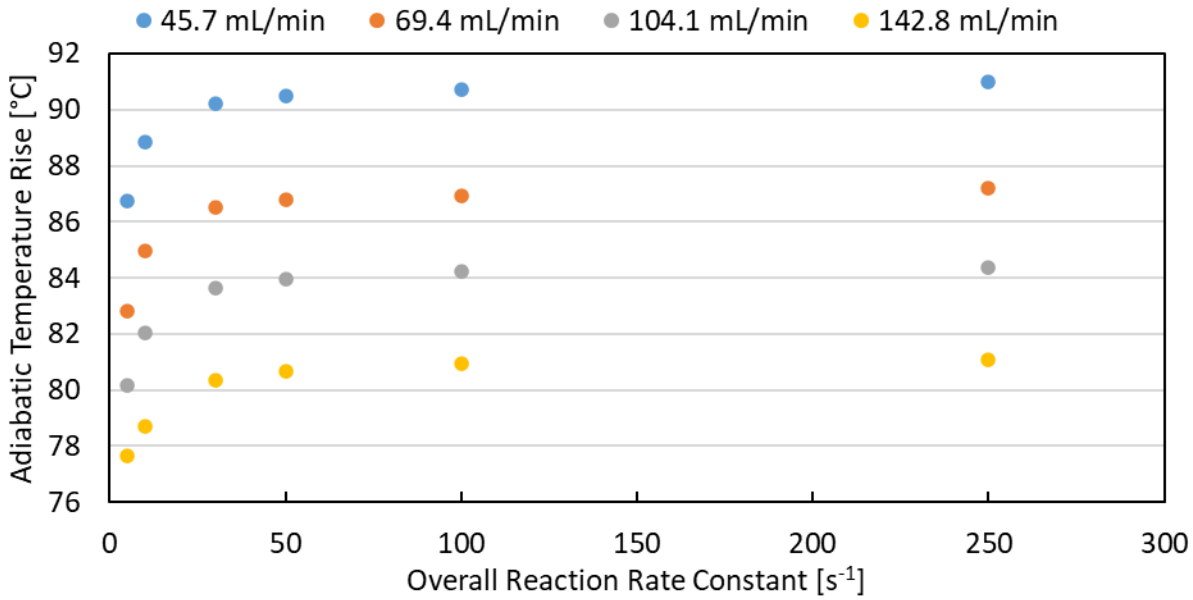

Fig. 3-7: Adiabatic temperature rise with respect to the overall reaction rate for all investigated flow rates.

While the adiabatic temperature rise is achieved with overall reaction rates greater than 30 s^{-1}, the heat of reaction between the different flow rates continues to differ. These deviations may be related to various experimental errors such as temperature probe accuracy (±1.5°C), errors in the local measurements of the overall heat transfer coefficient, and the reaction mass used to normalize

the heat of reaction. Further investigations are required to fully grasp the specific parameter which impacts the heat of reaction. However, the assumed local overall heat transfer coefficient profile at the inlet of the reactor is a likely contributor. Regardless, the heat of reaction remains quite similar between the flow rates with a maximum difference of 11.7%. The heat of reaction is found to be between -132.2 and -147.6 $kJ \cdot kg^{-1}$ for the LDA synthesis. See Table 3-3 for the full overview of the heat of reaction sensitivity to the overall reaction rate.

Table 3-3: Best fit heat of reaction as a function of the overall reaction rate evaluated at the four investigated flow rates. Using Fluitec's local overall heat transfer coefficient power-law regression.

	Heat of reaction [$kJ \cdot kg^{-1}$]			
Overall reaction rate [s^{-1}]	45.7 $mL \cdot min^{-1}$	69.4 $mL \cdot min^{-1}$	104.1 $mL \cdot min^{-1}$	142.8 $mL \cdot min^{-1}$
5	-142.8	-136.4	-131.9	-127.8
10	-146.2	-139.9	-135.1	-129.5
30	-148.5	-142.4	-137.7	-132.2
50	-149.0	-142.9	-138.2	-132.8
100	-149.3	-143.1	-138.6	-133.2
250	-149.8	-143.5	-138.9	-133.5
Average	**-147.6**	**-141.0**	**-136.6**	**-131.5**

The temperature profiles with respect to the different overall reaction rates are seen for the investigated flow rates in Fig. 3-8. The overall reaction rate is seen to impact the sharpness of the hotspot at the inlet of the reactor. This is expected as the overall reaction rate of the reactor increases resulting in the heat of reaction being released much faster than the convective heat transfer can remove it. After the reactors inlet, the temperature profile is seen to be identical for a given flow rate. Specifically, the model has great agreement with the first 200 millimeters of the reactor before starting to deviate from the experimental values. This can indicate that the values of the local overall heat transfer coefficient are too large at the outlet of the reactor resulting in a failure to match the experimental data. This observation is consistent with the sharp decrease in the local overall heat transfer coefficient seen earlier from the experimental data. In consequence, the fitted heat of reaction may be artificially increased as the optimization algorithm will attempt to minimize the residuals.

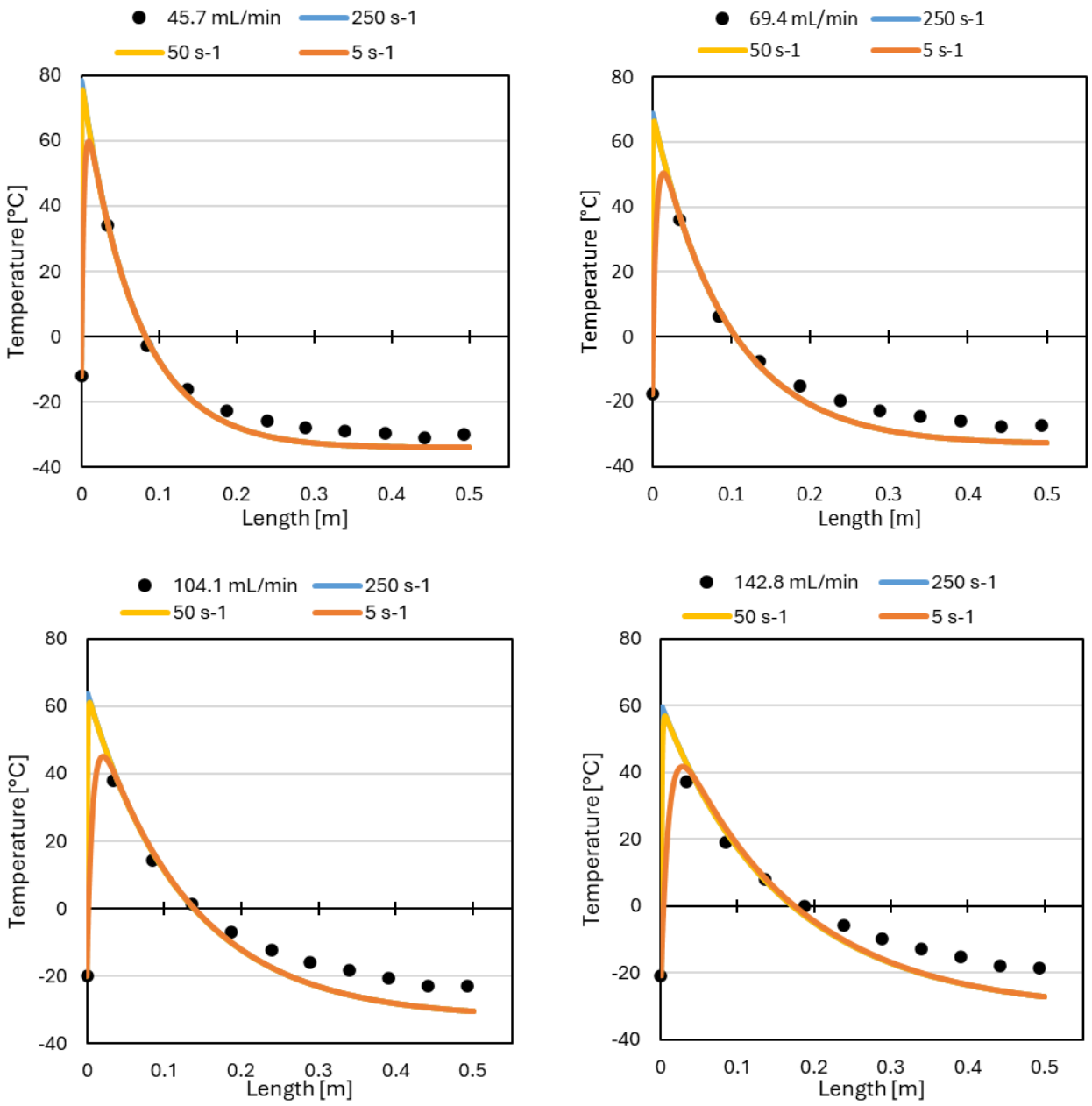

Fig. 3-8: Temperature profile of fitted heat of reaction for 5 s^{-1}, 50 s^{-1}, and 250 s^{-1} overall reaction rates. From left to right, top to bottom: 45.7 $mL \cdot min^{-1}$, 69.4 $mL \cdot min^{-1}$, 104.1 $mL \cdot min^{-1}$, 142.8 $mL \cdot min^{-1}$.

3.4.3.1. Discrete Energy Balance

An alternative methodology to determine the heat of reaction from the temperature profile in the calorimeter is to solve the energy balance in discrete segments. This method has been demonstrated by Mortzfeld et al.[44] Moser et al.[45], and Steinemann et al.[19] in past publications. By simplifying the energy balance to account for three effects, the heat flow of reaction (Q_r), the heat flow of mass

(Q_m), and the heat flow exchanged (Q_c) between the fluid and the jacket. The reactor is divided into equally spaced segments where the mass and exchanged heat flows are calculated in each segment. The fluid temperature is linearly interpolated between the temperature measurements. The local overall heat transfer coefficient is required to solve the Q_c in the segments.

$$0 = \frac{dQ}{dt} = Q_r - Q_c - Q_m; Q_r = Q_c + Q_m \tag{41}$$

$$Q_c = \sum_{i=1}^{n} UA_{s,i}\left(T_i - T_{\infty,i}\right) \tag{42}$$

$$Q_m = \sum_{i=1}^{n} \dot{m} C_p (T_i - T_{i-1}) \tag{43}$$

The heat flow of the reaction is determined by the addition of the mass and exchanged heat flow, closing the energy balance. The reaction heat flow must assume that all discrepancies between the mass and the exchanged heat flows are associated to the heat flow of reaction. One benefit of this methodology is that the energy balance does not require any reaction kinetics models or species balances to be solved. Thus, the heat of reaction can be estimated even if the reaction kinetics are unknown, see equation (44).

$$H_{rx} = \frac{Q_r}{\dot{m}} \tag{44}$$

Similar to the differential equation approach, characterizing the local variations in the overall heat transfer coefficient is essential, as the accuracy of the corresponding heat of reaction is dependent. However, solving the energy balance discretely introduces potential sources of error, as the energy balance closure is ensured by Q_r acting as a sink term. Consequently, the heat flow of reaction will conform to the temperature profile regardless of the accuracy of the local overall heat transfer coefficient. Additionally, the position of the peak temperature relative to the thermocouple temperature directly influences the accuracy of the calculated heat of reaction. This arises from the linear interpolation of the temperature profile between temperature measurements. This can be alleviated by increasing the resolution of the experimental temperature measurement. Provided that the spacing between the temperature measurements remains sufficient to prevent conductive thermal interference.

The heat of reaction was calculated using the discrete method as a direct comparison with the heat of reaction determined by the differential equation. The reactor length was divided into 1000 segments of equal length (0.5 mm). The local values for the overall heat transfer coefficient follow the power-law regression generated by Fluitec. The temperature profile and local variation of the overall heat transfer coefficient for the discrete method is demonstrated in Fig. 3-9.

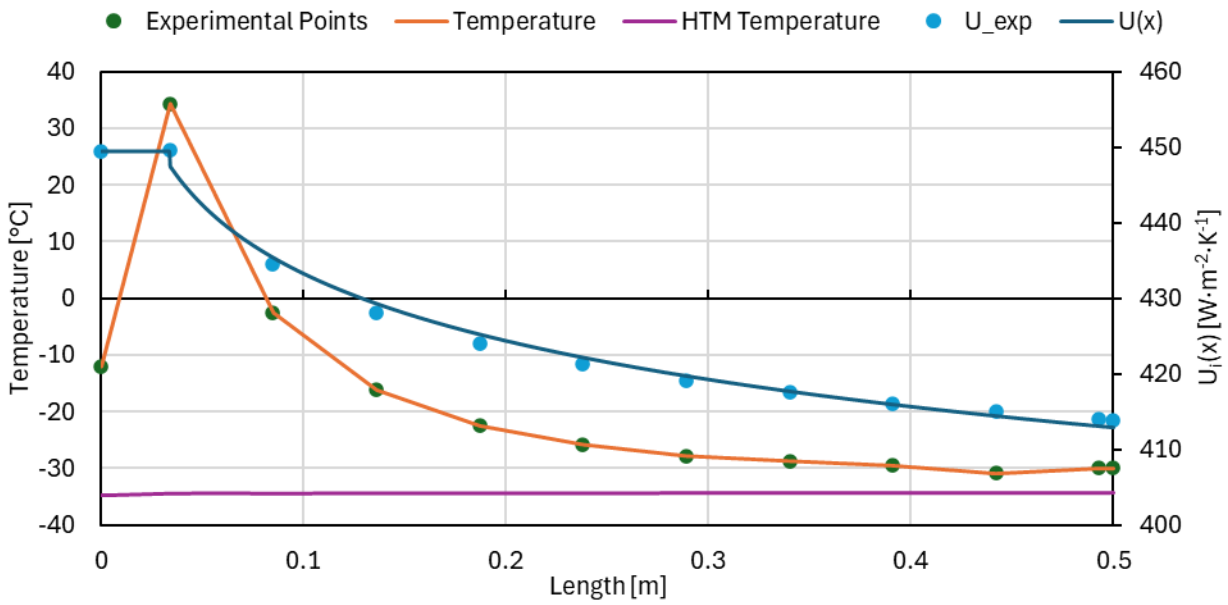

Fig. 3-9: Temperature profiles and local overall heat transfer coefficient at 45.7 mLmin^{-1} applying discrete energy balance methodology. Temperatures are linear interpolated between experimental points.

The associated heat of reactions obtained with the discrete approach are found to be higher on average by 11% than the heat of reactions found with the differential approach, see Table 3-4. One would suspect that the discrete approach would have a lower heat of reactions due to the lower peak temperature. However, this may be explained in part by the constant overall heat transfer coefficient at the reactor's inlet.

Table 3-4: LDA heat of reaction of discrete energy balance at investigated flow rates.

Flow rate [mL·min^{-1}]	Heat of reaction [kJ·kg^{-1}]
45.7	-155.9
69.4	-155.8
104.1	-154.4
142.8	-148.6

To better understand the impact of the local overall heat transfer coefficient the contribution of the heat flow associated with the reaction is plotted with respect to the reactor position, see Fig. 3-10. This trend demonstrates that roughly 70% of the chemical heat is found in the reaction zone, where the local overall heat transfer coefficient is kept constant. The remaining 30% of chemical energy is found to be outside the reactive zone. This increase in the Q_r contribution past the reactive zone suggests that the local overall heat transfer values are not adequate to close the energy balance. This discrepancy is consistent with the results found with the differential equation methodology as the energy balance failed to match the experimental temperature profile in the non-reactive segment.

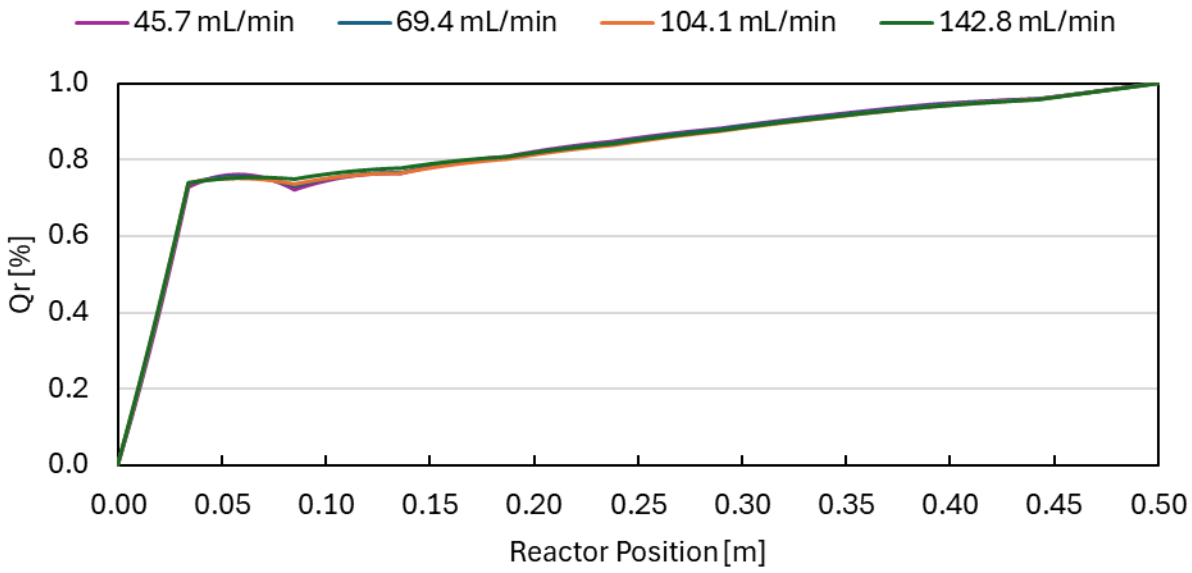

Fig. 3-10: Cumulative heat flow of reaction contribution with respect to the reactor position. All flow rates are plotted.

3.4.4. Continuous Calorimetry Limitations

Throughout this work, the heat of reaction for a type A reaction is determined using a continuous calorimeter as opposed to a conventional batchwise process. The continuous calorimeter ability to function with fast reaction times and unstable products has been crucial for the analysis. However, the limitations of technology cannot be ignored. One such limitation is the characterization work required ahead of performing heat of reaction determination. Specifically, regarding the mechanism for heat transfer. The local overall heat transfer coefficient, which may include the

conductive heat transfer resistance of the thermocouple and static mixers, must be well characterized to accurately measure the heat of reaction.

A difficulty with continuous calorimeters is the accurate measurement of the hotspot's peak temperature. The peak temperature and its profile are crucial for accurate heat of reaction estimates. However, to capture the peak temperature, the position of the thermocouple must be adjusted based on the given reaction. Furthermore, the fluids space time and reaction kinetics will have consequences on the position of the peak temperature. In practice, this can be alleviated by increasing the number of temperature measurements taken near the inlet of the reactor, decreasing the gap between the actual and measured peak temperature. Although, considerations must be made concerning the thermal interference that may occur between the measurements, and most importantly if such instrument can be procured.

In this work, the heat of reaction was determined by two distinct methodologies: solving the differential equations of the energy and species balances or solving the energy balance in a discrete manner. Both methodologies can estimate the heat of reaction, however, offer different advantages and limitations. Solving the energy balance as a system of ODEs requires the reaction's kinetic model, which may not be known. Increasing the experimentation time required to extract the heat of reaction as kinetic studies will need to be performed. On the other hand, the discrete method does not require any information on the kinetic model by coupling it to the energy balance. However, the method is heavily dependent on the temperature measurements and their relative position to the hotspot. Furthermore, the temperature profile must be interpolated as this is a required input for the methodology. Ultimately, either methodology is suitable; however, the best approach is dependent on the specific constraints and available data on the investigated reaction. Nevertheless, accurate estimates of the local overall heat transfer data are required when determining the heat of reaction.

Although, if the energy balance is solved discretely, the calorimeter must be operated under conditions that maintain a complete conversion before exiting the reactor. Otherwise, the heat generated (or consumed) by the chemical reaction will not be fully encompassed in the temperature profile. Impacting the heat of reaction calculated by the discrete approach. Otherwise, the differential equation methodology can be applied to obtain the heat of reaction regardless of the conversion achieved.

3.5. Conclusions

The heat of reaction for the synthesis of lithium diisopropylamine (LDA) from n-butyllithium (nBuLi) and diisopropylamine (DIPA) has been determined with a continuous calorimeter. A continuous calorimeter is preferred over a conventional batchwise process, for the synthesis of LDA, as the LDA suffers from stability and degradation issues which are ill-suited for this approach.

The energy and species balances of the continuous calorimeter were solved with a MATLAB® simulation. To obtain the synthesis heat of reaction, three other parameters had to be determined: the local overall heat transfer coefficient throughout the reactor, the overall reaction rate, and the fluid axial thermal conductivity. The fluid axial thermal conductivity in the calorimeter was determined to be negligible by the sensitivity analysis performed. This was achieved, by segmenting the reactor in two, a reactive and non-reactive zone, and performing a two-parameter fit on the average overall heat transfer coefficient and the fluid axial thermal conductivity.

The local overall heat transfer coefficient of the continuous calorimeter was determined using experimental temperature profile data from the non-reactive zone. The analysis revealed significant variation in the local overall heat transfer coefficient along the reactor length, suggesting that one or more thermal resistances undergo substantial change. Given that the inner and outer convective heat transfer resistances are expected to remain relatively constant beyond the developing region near the reactor inlet, this variation may instead arise from non-negligible conductive heat transfer resistances associated with the static mixers and thermocouple rod solid phase. However, due to insufficient geometric details regarding the thermocouple construction and the complex geometry of the static mixers, a comprehensive assessment of these resistances could not be performed. Future work should incorporate a three-dimensional multiphase energy balance on the solid (static mixers and thermocouple) and fluid phases to investigate the underlying cause of the heat transfer coefficient variation. Requiring a CFD simulation to solve the complex geometry, three-dimensional local conservations equations, and the multiphase aspects of the continuous calorimeter. In the absence of such data, empirical correlations supplied by the calorimeter and static mixer manufacturer were employed to estimate the local overall heat transfer coefficients. Nevertheless, regardless of the methodology used to determine the heat of reaction, the derived coefficients failed to yield an accurate fit with the experimental data. This discrepancy

is evident in the differential equation approach, where the simulated temperature profiles deviated from experimental measurements, as well as in the discrete approach, where the calculated heat flow of reaction (Q_r) did not achieve closure past the reaction zone.

The heat of reaction was determined by investigating its sensitivity with the overall reaction rate. The overall reaction rates investigated are chosen such that the second Damköhler number is greater than one, keeping the mixing rate governing. The sensitivity analysis identified that past an overall reaction rate of 30 s^{-1} the adiabatic temperature rise is reached in the reactor, keeping the fitted heat of reaction constant. The fitted heat of reaction by the simulation is estimated to be between -132 $kJ \cdot kg^{-1}$ and -148 $kJ \cdot kg^{-1}$, corresponding to an adiabatic temperature rise of 90.9°C and 81.2°C based on the investigated flow rates. The range of heat of reaction values is presumed to be associated with the accuracy of the local overall heat transfer coefficient and the extrapolation assumed in the developing region.

4. Conclusions and Future Work

In this thesis, continuous flow chemistry processes for applications in the pharmaceutical industry were investigated to produce active pharmaceuticals ingredients (APIs). The continuous processes were focused on organolithium reaction characterized by their fast reaction kinetics resulting in mixing controlled reactions, and high exothermicities requiring highly optimized temperature control and reactant stoichiometry to minimize selectivity losses. The main objectives of this work were to characterize the transport phenomena (frictional pressure loss, inner heat transfer, and residence time distribution) of a continuous shell and tube reactor and investigate the heat of reaction for the synthesis of lithium diisopropylamine (LDA) from nBuLi and DIPA in a continuous flow calorimeter featuring inline temperature measurements.

In chapter 2, the empirical correlation of the friction factor and inner tube Nusselt number were generated for reactor tube featuring Kenics® mixers with diameters of 3.05 mm which have not been reported previously in literature. Both correlations accurately fit the experimental data in the range of hydraulic Reynolds number and Prandtl numbers investigated. The hydraulic Reynolds number is varied between 200 and 4500 while the Prandtl number ranges between 4.6 and 7.0. The correlation average absolute relative error for the friction factor and inner Nusselt number are 5% and 23%, respectively. The characterization of the heat transfer and frictional pressure drop found that the reactors flow regime was laminar for hydraulic Reynolds numbers below 500 and reached a fully turbulent regime when the hydraulic Reynolds passed 2500. Future works should consider broadening the friction factor and Nusselt number correlation to include different static mixer designs, tube diameters, and fluid properties.

The residence time distribution characterization found that the reactor operates effectively in plug flow conditions as the Peclet number surpasses the threshold value of 100. The near plug flow behavior is maintained regardless of the power dissipation investigated. This corresponds to a power dissipation ranging from 0.15 $W \cdot kg^{-1}$ to 1.6 $W \cdot kg^{-1}$. The reactor's RTD profile is modelled with the axial dispersion model with an AARE of 11%. However, during the deconvolution of the inlet and outlet step-change signals, it was noticed that some dimensionless variance decreased from the inlet to the outlet when the power dissipation was greater than 0.35 $W \cdot kg^{-1}$. This result is physically impossible as the variance increases proportionally with length ($\sigma^2 \propto L$). This error was identified and associated with the Coriolis response time of the density measurements.

Nevertheless, the dimensionless variance obtained at the inlet and outlet of the reactor combined with the step-change profile suggested the near plug flow behavior of the reactor. Future works investigating the RTD of the reactor should decrease the instruments response time by either improving the Coriolis or using spectroscopic techniques. These modifications will allow for greater power dissipation to be investigated and may indicate a relationship between the power dissipation and Peclet number.

Power dissipation scale-up demonstrates the relationship between the frictional pressure drop and heat transfer transport phenomena. The frictional pressure drop was seen to increase with power dissipation in a consistent manner regardless of the tube diameters when the first Damköhler number is kept constant by adjusting the reactor's length. Maintaining a constant Da_I ensures the reactions extents are similar at increased scales. While the inner heat transfer coefficient ratio was shown to remain nearly identical when the power dissipation is kept constant by adjusting the tube diameter and flow rates. Nevertheless, the loss surface-to-volume with scale-up was identified by contrasting the inner heat transfer coefficient with the volumetric inner heat transfer coefficient. This comparison demonstrated the clear loss in convective heat transfer due to increasing tube diameters. Solutions to alleviate these concerns are proposed, such as the multi-injection principle to fractionate the heat load along the reactor length and numbering up the process by having multiple reactors in parallel.

In chapter 3, the heat of reaction for the synthesis of LDA from n-butyllithium (nBuLi) and diisopropylamine (DIPA) is found to be between -132 $kJ \cdot kg^{-1}$ and -148 $kJ \cdot kg^{-1}$ in the continuous calorimeter. A continuous calorimetry was chosen for the organolithium reaction as it suffers from stability and degradation concerns in addition to being ill-suited for conventional batchwise processes. The heat of reaction is obtained by solving the energy and species balances with a MATLAB® simulation. The energy balance is one-dimensional in the axial direction, assuming steady-state conditions, applied on the fluid phase. It accounts for the thermal conductivity of the fluid, and the convective cooling between the jacket fluid and inner tube. The local overall heat transfer coefficient in the energy balance is normalized on the inner tube area. The fluid axial thermal conductivity was determined to be insignificant in the continuous calorimeter by performing a sensitivity analysis between it and the convective heat transfer. The local overall heat transfer coefficient of the reactor was found to vary substantially along the length of the reactor,

suggesting that one or more thermal resistances must undergo substantial change. Given that the inner and outer convective heat transfer resistances are expected to remain relatively constant beyond the developing region near the reactor inlet, this variation may instead arise from non-negligible conductive heat transfer resistances associated with the static mixers and thermocouple rod. However, due to insufficient geometric details regarding the thermocouple construction and the complex geometry of the static mixers, a comprehensive assessment of these resistances could not be performed. Future work should incorporate a three-dimensional multiphase energy balance on the solid (static mixers and thermocouple) and fluid phases to investigate the underlying cause of the local overall heat transfer coefficient variation. Requiring a CFD simulation to solve the complex geometry, three-dimensional local conservation equations, and the multiphase aspects of the continuous calorimeter. In the absence of such an analysis, the calorimeter and static mixer manufacturer provided empirical correlations and values for the local overall heat transfer coefficient. Nevertheless, the derived coefficients failed to yield an accurate fit of the experimental temperature profile with the MATLAB® simulation. This discrepancy was independently validated by calculating the heat of reaction in a discrete approach by simplifying the energy balance. The sensitivity of the heat of reaction was investigated by adjusting the overall reaction rate. The overall reaction rate values were chosen such that the second Damköhler number ensures the mixing rate is governing. This analysis found that past an overall reaction rate of 30 s^{-1}, the adiabatic temperature rise was achieved. Corresponding to 90.9°C and 81.2°C from the lowest to highest investigated flow rates.

5. References

[1] M. Baumann, T. S. Moody, M. Smyth, S. Wharry, *Org. Process Res. Dev.* **2020**, *24*, 1802.
[2] L. Malet-Sanz, F. Susanne, *J. Med. Chem.* **2012**, *55*, 4062.
[3] B. J. Doyle, P. Elsner, B. Gutmann, O. Hannaerts, C. Aellig, A. Macchi, D. M. Roberge, *Org. Process Res. Dev.* **2020**, *24*, 2169.
[4] M. Baumann, I. R. Baxendale, *Beilstein J. Org. Chem.* **2015**, *11*, 1194.
[5] G. Fu, J. Jiang, C. A. Hone, C. Oliver Kappe, *Reaction Chemistry & Engineering* **2023**, *8*, 577.
[6] B. Gutmann, D. Cantillo, C. O. Kappe, *Angewandte Chemie International Edition* **2015**, *54*, 6688.
[7] S. G. Kandlikar, *Heat transfer and fluid flow in minichannels and microchannels*, Second edition., Butterworth-Heinemann, Amsterdam, **2014**.
[8] M. Power, E. Alcock, G. P. McGlacken, *Org. Process Res. Dev.* **2020**, *24*, 1814.
[9] R. Porta, M. Benaglia, A. Puglisi, *Org. Process Res. Dev.* **2016**, *20*, 2.
[10] R. L. Hartman, J. P. McMullen, K. F. Jensen, *Angewandte Chemie International Edition* **2011**, *50*, 7502.
[11] J. A. Bennett, Z. S. Campbell, M. Abolhasani, *Current Opinion in Chemical Engineering* **2019**, *26*, 9.
[12] E. Mielke, P. Plouffe, N. Koushik, M. Eyholzer, M. Gottsponer, N. Kockmann, A. Macchi, D. M. Roberge, *React. Chem. Eng.* **2017**, *2*, 763.
[13] R. A. (Tony) Taylor, W. R. Penney, H. X. Vo, *Ind. Eng. Chem. Res.* **2005**, *44*, 6095.
[14] N. Kockmann, M. Gottsponer, D. M. Roberge, *Chemical engineering journal (Lausanne, Switzerland : 1996)* **2011**, *167*, 718.
[15] D. M. Roberge, *Org. Process Res. Dev.* **2004**, *8*, 1049.
[16] D. M. Roberge, L. Ducry, N. Bieler, P. Cretton, B. Zimmermann, *Chemical Engineering & Technology* **2005**, *28*, 318.
[17] P. Plouffe, A. Macchi, D. M. Roberge, *Organic process research & development* **2014**, *18*, 1286.
[18] P. Barthe, C. Guermeur, O. Lobet, M. Moreno, P. Woehl, D. M. Roberge, N. Bieler, B. Zimmermann, *Chemical Engineering & Technology* **2008**, *31*, 1146.
[19] F. L. Steinemann, D. P. Rütti, M. Moser, A. G. Georg, D. M. Meier, *J Flow Chem* **2022**, *12*, 389.
[20] N. Kockmann, D. M. Roberge, *Chemical engineering and processing* **2011**, *50*, 1017.
[21] V. Nuredin, L. Schulz, N. Kockmann, T. Röder, *J Flow Chem* **2025**, *15*, 47.
[22] O. Levenspiel, *Chemical reaction engineering*, John Wiley & Sons, New York, **1999**.
[23] *Perry's Chemical Engineers' Handbook*, D. W. Green, M. Z. Southard, Eds., 9th Edition., McGraw-Hill Education, **2019**.
[24] M. Hosni, M. Hammoudi, E.-K. Si-Ahmed, J. Legrand, L. Douib, *Canadian journal of chemical engineering* **2023**, *101*, 828.
[25] V. Kumar, V. Shirke, K. D. P. Nigam, *Chemical engineering journal (Lausanne, Switzerland : 1996)* **2008**, *139*, 284.
[26] J. Sbreve]IR, Z. LECJAKS, *Chemical engineering communications* **1982**, *16*, 325.
[27] P. Joshi, K. D. P. Nigam, Eb. Nauman, *The Chemical engineering journal and the biochemical engineering journal* **1995**, *59*, 265.
[28] W. D. Morris, J. Benyon, *Ind. Eng. Chem. Proc. Des. Dev.* **1976**, *15*, 338.
[29] H.-S. Song, S. P. Han, *Chemical engineering science* **2005**, *60*, 5696.

[30] P. R. Patil, G. G. Dastane, A. B. Pandit, *Heat Transfer* **2024**, *53*, 44.
[31] X. Jiang, Z. Xiao, J. Jiang, X. Yang, R. Wang, *Chemical Engineering Journal* **2021**, *424*, 130399.
[32] N. Kockmann, D. M. Roberge, *Chemical engineering & technology* **2009**, *32*, 1682.
[33] Fogler Scott H., Vennema Catherine, Vennema Ame, Thurnau Arthur F., *Elements of Chemical Reaction Engineering*, Prentice Hall, Boston, **2016**.
[34] M. M. Fadaee, B. J. Doyle, D. M. Roberge, A. Macchi, J. B. Haelssig, *Chemical engineering journal (Lausanne, Switzerland : 1996)* **2024**, *492*, 151758.
[35] E. L. Paul, V. A. Atiemo-Obeng, S. M. Kresta, North American Mixing Forum, *Handbook of industrial mixing: science and practice*, Wiley-Interscience, Hoboken, N.J, **2004**.
[36] C. A. Hone, C. O. Kappe, *Chemistry–Methods* **2021**, *1*, 454.
[37] J. R. Bourne, *Organic process research & development* **2003**, *7*, 471.
[38] N. Kockmann, *Transport Phenomena in Micro Process Engineering*, Heat and Mass Transfer, 1st ed. 2008., Springer Berlin Heidelberg, Berlin, Heidelberg, **2008**.
[39] D. M. Roberge, N. Bieler, M. Mathier, M. Eyholzer, B. Zimmermann, P. Barthe, C. Guermeur, O. Lobet, M. Moreno, P. Woehl, *Chemical engineering & technology* **2008**, *31*, 1155.
[40] G. H. Chen, Z. L. Liu, *Advanced Materials Research* **2013**, *694–697*, 547.
[41] O. Naaman, J. Aumentado, *Physical review letters* **2006**, *96*, 100201.
[42] S. M. Sarge, *Calorimetry: fundamentals, instrumentation and applications*, Wiley-VCH, Weinheim, **2014**.
[43] W. Litz, *Bench scale calorimetry in chemical reaction kinetics: an alternative approach to liquid phase reaction kinetics*, Springer, Cham, **2015**.
[44] F. Mortzfeld, J. Polenk, B. Guelat, F. Venturoni, B. Schenkel, P. Filipponi, *Organic process research & development* **2020**, *24*, 2004.
[45] M. Moser, A. G. Georg, F. L. Steinemann, D. P. Rütti, D. M. Meier, *J Flow Chem* **2021**, *11*, 691.
[46] A. Ładosz, C. Kuhnle, K. F. Jensen, *React. Chem. Eng.* **2020**, *5*, 2115.
[47] C. Hany, H. Lebrun, C. Pradere, J. Toutain, J.-C. Batsale, *Chemical Engineering Journal* **2010**, *160*, 814.
[48] F. Reichmann, K. Vennemann, T. A. Frede, N. Kockmann, *Chemie Ingenieur Technik* **2019**, *91*, 622.
[49] F. Reichmann, S. Millhoff, Y. Jirmann, N. Kockmann, *Chemical Engineering & Technology* **2017**, *40*, 2144.
[50] G. Glotz, D. J. Knoechel, P. Podmore, H. Gruber-Woelfler, C. O. Kappe, *Org. Process Res. Dev.* **2017**, *21*, 763.
[51] M. C. Maier, M. Leitner, C. O. Kappe, H. Gruber-Woelfler, *React. Chem. Eng.* **2020**, *5*, 1410.
[52] J. Lerchner, A. Wolf, G. Wolf, V. Baier, E. Kessler, M. Nietzsch, M. Krügel, *Thermochimica acta* **2006**, *445*, 144.
[53] J. S. Zhang, C. Y. Zhang, G. T. Liu, G. S. Luo, *Chemical Engineering Journal* **2016**, *295*, 384.
[54] T. L. Bergman, A. S. Lavine, F. P. Incropera, D. P. DeWitt, *Fundamentals of Heat and Mass Transfer*, 8th Edition., Wiley, **2019**.
[55] A. Nagaki, Y. Ashikari, M. Takumi, T. Tamaki, *Chemistry Letters* **2021**, *50*, 485.

[56] D. B. Collum, A. J. McNeil, A. Ramirez, *Angewandte Chemie International Edition* **2007**, *46*, 3002.
[57] R. L. Rowley, W. V. Wilding, J. L. Oscarson, Y. Yang, N. A. Zundel, T. E. Daubert, R. P. Danner, DIPPR Data Compilation of Pure Chemical Properties **2007**.